S3 HTHH-MOC model validation and analysis results

S3.1 Evolution of water and aerosol plumes (Exp2)

Authors Valentina Aquila
Adam Bourassa
Sergey Khaykin
Alexandre Baron
Landon Rieger
Alexei Rozanov
Rei Ueyama

Contributors Slimane Bekki
Ewa M. Bednarz
Christoph Brühl
Parker Case
Simon Chabrillat
Margot Clyne
Peter R. Colarco
Lola Falletti
Nicolas Lebas
Cheng-Cheng Liu
Marion Marchand
Yifeng Peng
Samuel Rémy
Takashi Sekiya
Simone Tilmes
Xinyue Wang
Shingo Watanabe
Pengfei Yu
Wandi Yu
Jun Zhang
Yunqian Zhu
Zhihong Zhuo

While the figures in Chapter 3 focus on the comparison between Exp2a simulations and observations, the figures in the supplementary material help the analysis of the model simulations and the characterisation of the behaviour of models by showing, for instance, results for the simulated background conditions.

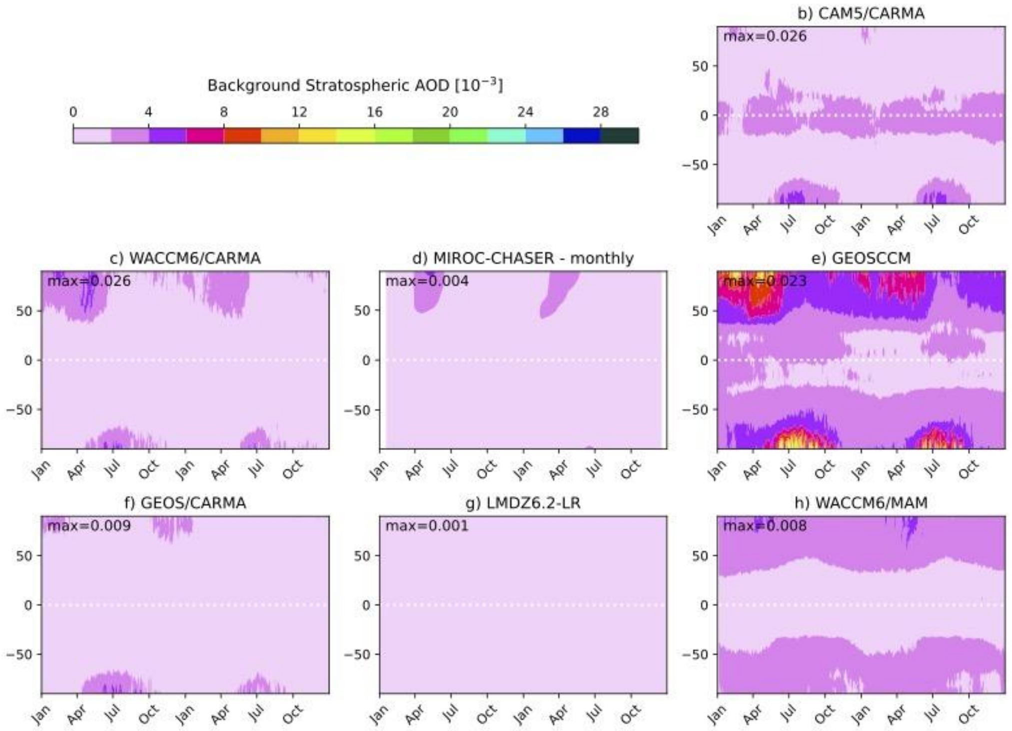

Figure S3.1: *Zonal mean background near-IR SAOD in the Exp2a models, as simulated in the experiment without Hunga injection. The SAOD of all models was calculated based on daily values, except for MIROC-CHASER which was calculated based on monthly means. The upper left value indicates the maximum SAOD value.*

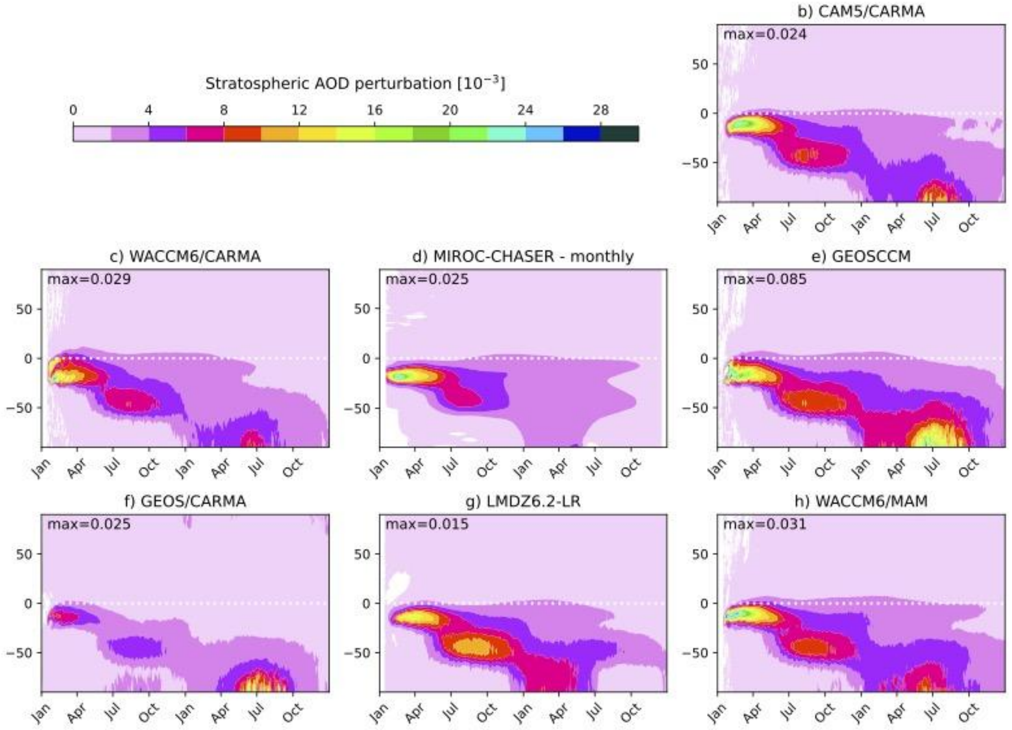

Figure S3.2: *Simulated zonal mean near-IR SAOD perturbation as a function of time and latitude in different global climate models, calculated as the difference between the simulation with and without Hunga. The SAOD of all models was calculated based on daily values, except for MIROC-CHASER and EMAC MPIC which only provided monthly means. The number in the upper left indicates the maximum value.*

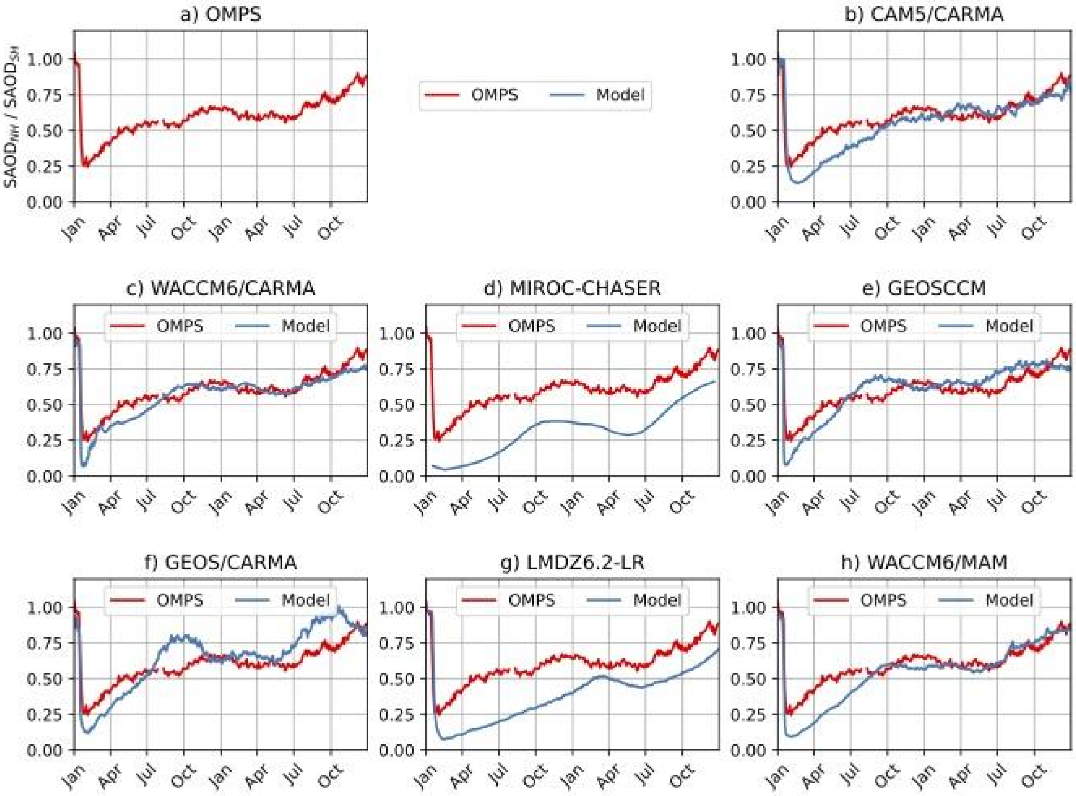

Figure S3.3: *Ratio of the average SAOD between Equator–20°N to SAOD between Equator–20°S in the Exp2a models (blue) and OMPS observations (red). The simulated ratio is lower than the observed one, indicating that models underestimate the SAOD in the northern tropics and therefore the cross-equatorial transport.*

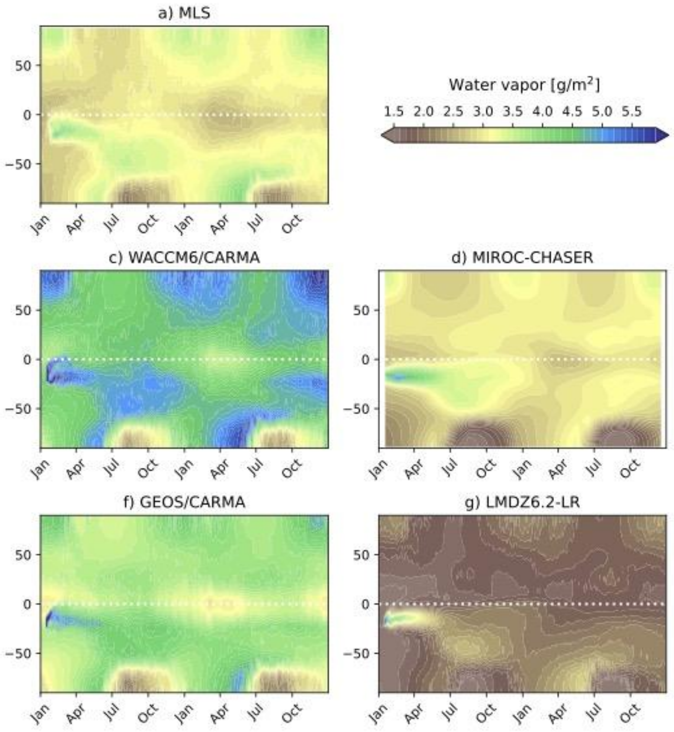

Figure S3.4: *Zonal mean stratospheric water vapour column in MLS water vapour and in the Exp2a simulation with the Hunga eruption. The simulated stratospheric water column is calculated above 100 hPa.*

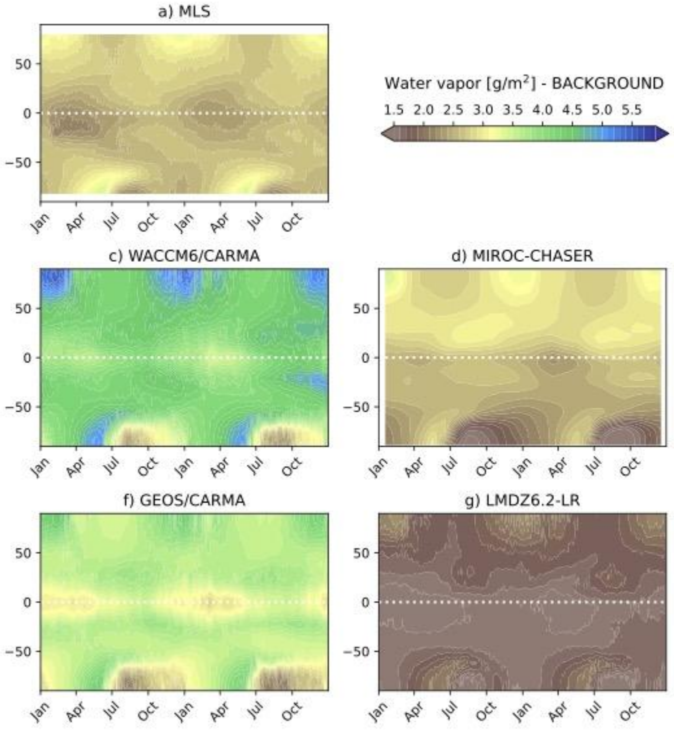

Figure S3.5: *Zonal mean stratospheric water vapour column in the MLS climatology calculated over 2005–2021 and the Exp2a simulation without the Hunga eruption. The simulated stratospheric water column is calculated above 100 hPa.*

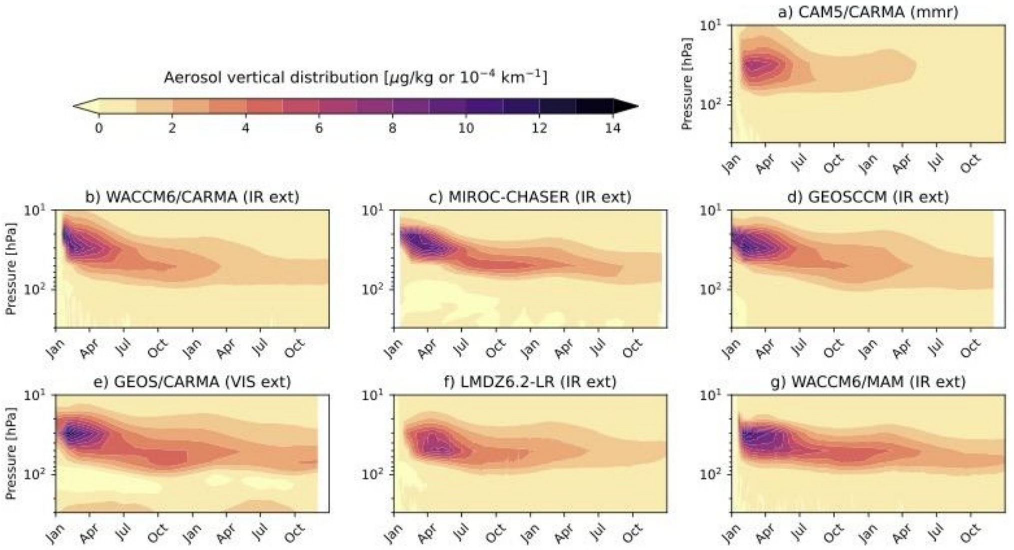

Figure S3.6: *Zonal mean aerosol perturbation as a function of time and altitude averaged over 30°S to 30°N in Exp2a simulations. Shown are the extinction coefficients (in 10^{-4} km^{-1}) in the near-IR range for all models except for GEOS/CARMA (e), which reports the extinction in the visible range, and CAM5/CARMA (a), which reports the sulfate mass mixing ratio (in μg kg^{-1}). Perturbations are based on daily values, except for MIROC-CHASER, which were calculated from monthly means.*

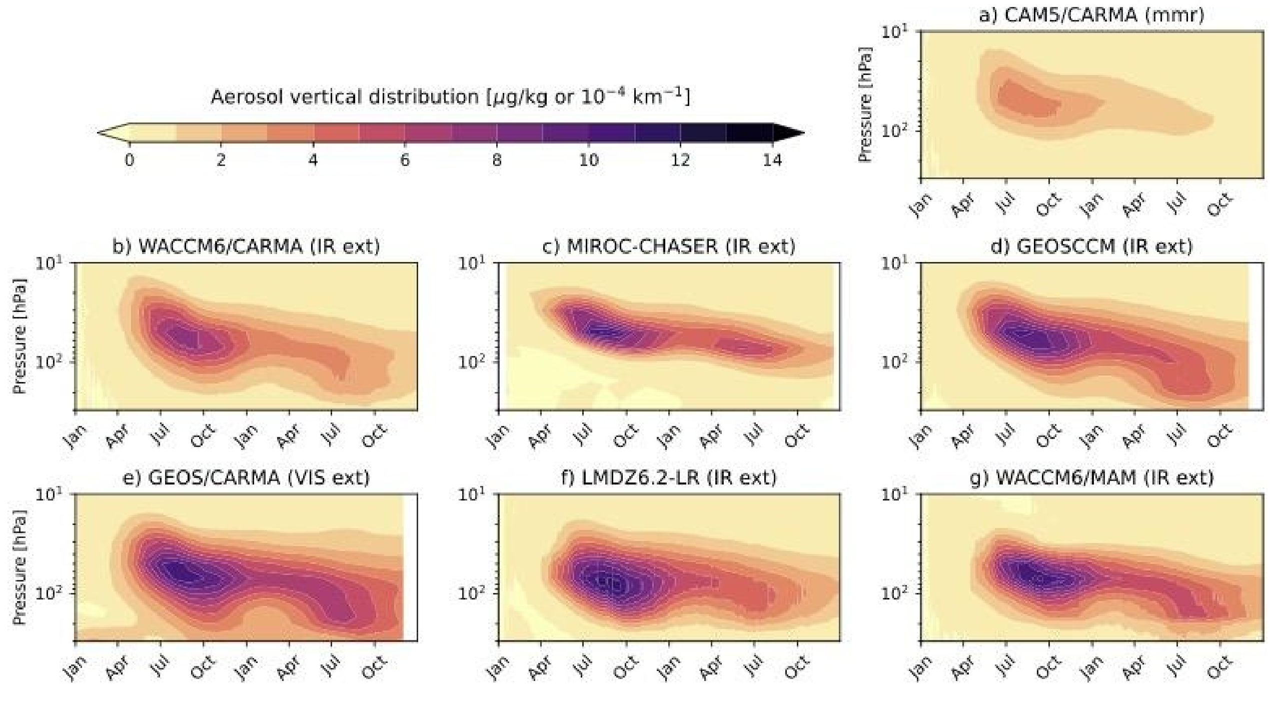

Figure S3.7: *As for Figure S3.6, but for 30°S to 60°S.*

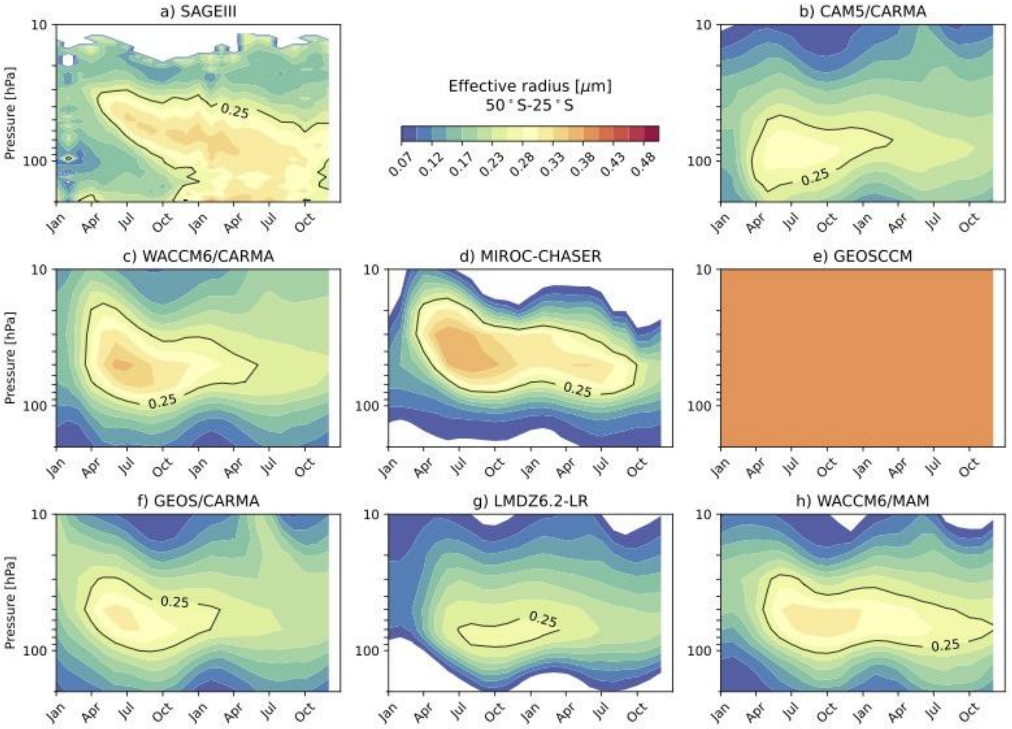

Figure S3.8: *Monthly mean aerosol effective radius averaged over the southern midlatitudes (25°S–50°S) as a function of time and altitude in SAGE III/ISS and in Exp2a models from January 2022 to December 2023. GEOSCCM is a bulk model and assumes a constant effective radius equal to 0.4 μm.*

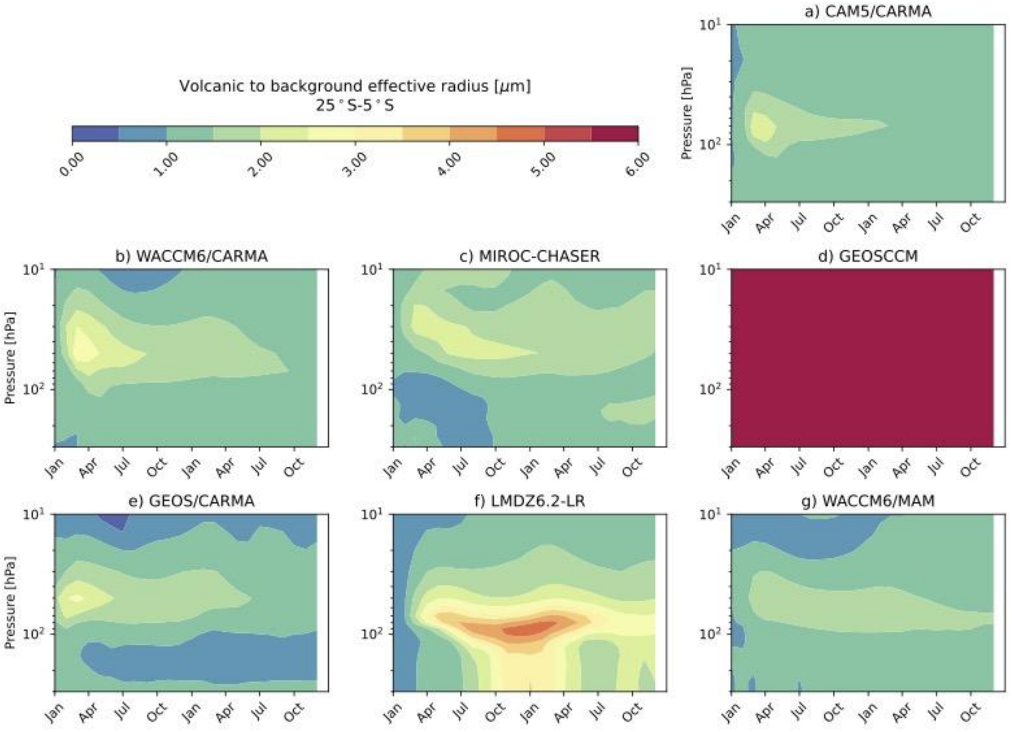

Figure S3.9: *Ratio between the monthly mean aerosol effective radius in the Exp2a simulation with and without Hunga eruption, averaged over 5°S–25°S. GEOSCCM is a bulk model and assumes a constant effective radius equal to 0.4 μm for the Hunga aerosols and 0.069511 μm for the background aerosols.*

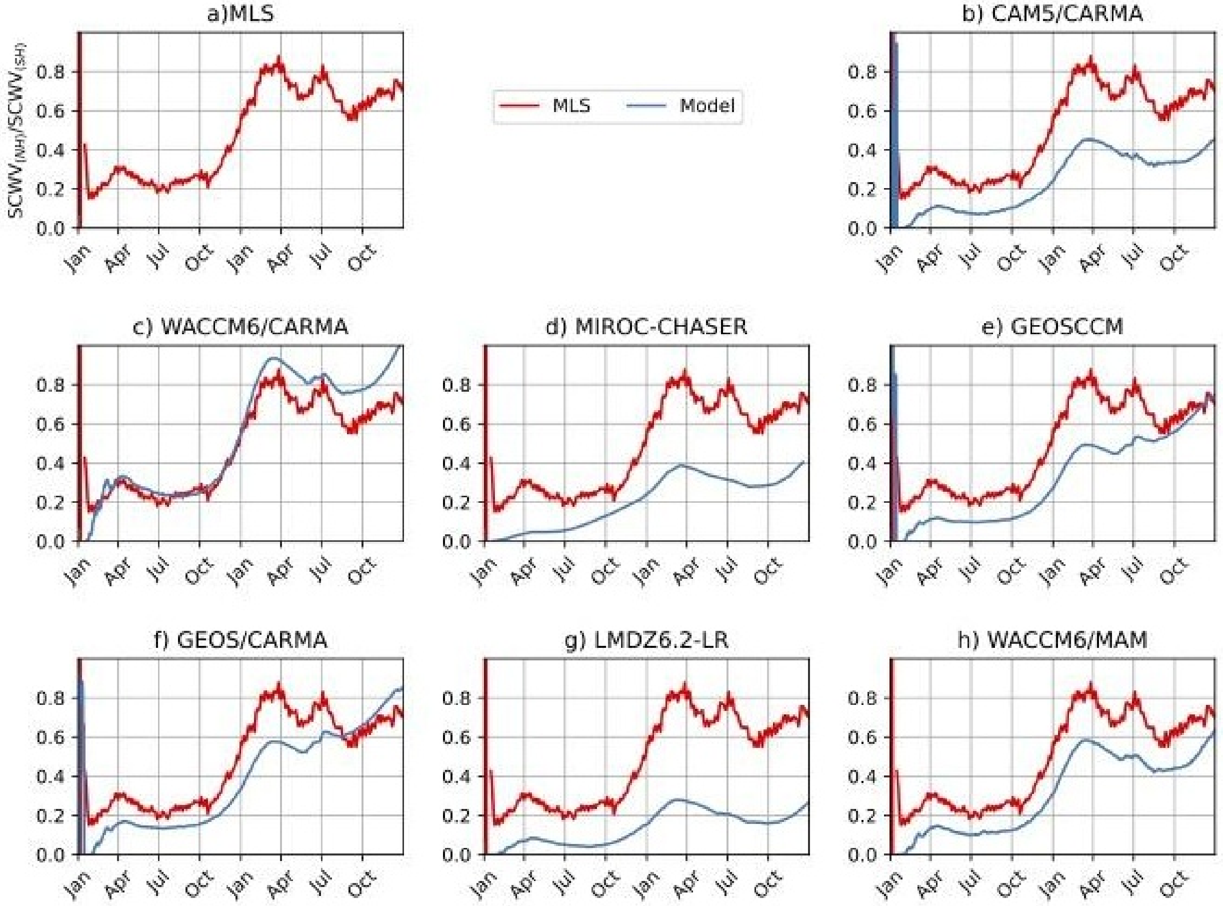

Figure S3.10: *Ratio between the mean stratospheric water vapour column in the northern hemisphere (equator–90°N) to the one in the southern hemisphere (equator–90°S) in MLS observations (red) and in Exp2a models (blue). Except for WACCM6/CARMA (c), all models underestimate the cross-equatorial transport of water vapour.*

S3.2 Hunga plumes evolution and stratospheric responses (based on EXP1 10-year output analysis)

Authors Zhihong Zhuo
Xinyue Wang
Yunqian Zhu
Wandi Yu
Ewa M. Bednarz
Eric Fleming
Peter R. Colarco
Shingo Watanabe
David Plummer
Georgiy Stenchikov
William Randel
Adam Bourassa
Valentina Aquila
Takashi Sekiya
Mark R. Schoeberl
Simone Tilmes
Jun Zhang
Paul J. Kushner
Francesco S. R. Pausata

This section is based on: Zhu et al. (2025).

Zhuo, Z., Wang, X., Zhu, Y., Yu, W., Bednarz, E. M., Fleming, E., Colarco, P. R., Watanabe, S., Plummer, D., Stenchikov, G., Randel, W., Bourassa, A., Aquila, V., Sekiya, T., Schoeberl, M. R., Tilmes, S., Zhang, J., Kushner, P. J., and Pausata, F. S. R.: Comparing multi-model ensemble simulations with observations and decadal projections of upper atmospheric variations following the Hunga eruption, *Atmos. Chem. Phys.*, 25, 13161–13176, `https://doi.org/10.5194/acp-25-13161-2025`, 2025.

Multi-model ensemble and observation comparison using all available model simulations in Exp1 (coupled ocean and fixed SSTs), GloSSAC, OMPS, and MLS data.

S3.2.1 Stratospheric aerosol optical depth (SAOD) anomaly

GloSSAC data indicate that the volcanic aerosols are predominantly concentrated in the Southern Hemisphere (SH), with a smaller fraction transported to the Northern Hemisphere (NH) tropics (Figure S3.11). In the first few months of 2022, the aerosols remain largely trapped in the low latitudes of the tropical pipe (Taha et al., 2022). The SH (0–30°S) experiences a higher aerosol concentration compared to the NH tropics (0–30°N). From mid-2022, during the austral winter, more aerosols are transported to the SH mid-latitudes (30°-60°S). The strong polar vortex in the austral winter and spring prevents further poleward transport (Manney et al., 2023). However, at the end of 2022 and the beginning of 2023, the break-up of the polar vortex during austral late spring-early summer allows for a slight poleward movement of aerosols toward the southern polar regions, with a minor portion also being transported northward toward the tropics. Following this, the aerosols are predominantly confined and transported in the SH mid-latitudes. This pattern reflects the influence of seasonal changes in the polar vortex and the Brewer-Dobson circulation on stratospheric aerosol transport (Butchart, 2014). OMPS observations show a similar latitudinal transport pattern over time, although exhibit stronger SAOD values in the tropics and southern mid-latitudes compared to GloSSAC.

Model simulations demonstrate reasonable agreement with observed latitudinal SAOD distribution patterns (Figure S3.11). Both GloSSAC and OMPS show a decrease in SAOD over time as aerosols are transported toward SH high latitudes. WACCM6MAM-co, WACCM6MAM-fs, and MIROC-CHASER-fs all exhibit similar trends, though with stronger SAOD in the tropics compared to observations. In contrast, GEOSCCM-fs displays weaker SAOD in the tropics and stronger SAOD in the polar regions (60–90°S) by mid-2023 compared to mid-latitudes (30–60°S) in mid-2022. Additionally, models show that the anomaly diminishes mostly by the end of 2024. These differences may stem from uncertainties in both modelling and satellite observation, including variations in simulated aerosol microphysics and dynamics, as well as uncertainties in aerosol estimates from GloSSAC and OMPS retrievals. Understanding these differences and uncertainties is a key objective of the Tonga Model Intercomparison Project (Tonga-MIP; Clyne et al., 2024), which, as a parallel initiative, will also contribute to the Hunga Assessment Report (Zhu et al., 2025).

Both observational data and model simulations show that the SAOD anomaly induced by the Hunga eruption lasts for approximately two years in the SH low latitudes. Additionally, both sources are consistent in identifying a secondary peak in SAOD over SH mid-latitudes during the second austral winter in 2023. Model projections further suggest minor extensions of the SAOD anomaly into the third and fourth years in SH high latitudes, with the third-year signal being particularly robust across climate models and also independent of ocean–atmosphere coupling.

S3.2.2 Water vapour variation

Global stratospheric water vapour (SWV) mass anomaly The Hunga eruption led to an unprecedented increase in stratospheric water vapour (SWV), significantly influencing global SWV loading. After removing background water vapour, the MLS-observed SWV mass anomaly from the Hunga eruption initially stabilised at approximately 135 Tg before beginning to decline in the spring of 2023 (Figure S3.12). Following a slight increase in late 2023, it began decreasing more rapidly in early 2024, reaching approximately 70 Tg by the end of 2024. The initial SWV mass analyzed based on the v5 retrieval of MLS is slightly lower than previous estimates using the v4 retrieval, which indicated a ~150 Tg water vapour injection by the Hunga eruption (Carr et al., 2022; Millán et al., 2022).

Compared to MLS observations, the modelled SWV mass anomalies exhibit varying evolutionary trends. WACCM6MAM-co and WACCM6MAM-fs replicate the MLS observations well, with an initial mass of approximately 135–140 Tg and a continuous plateau in SWV mass before it begins decreasing in early 2023. Despite an initial injection mass of 150 Tg, the rapid reduction of 10–15 Tg is attributed to the water vapour saturation effect, which converts water vapour into ice clouds during the first week after injection, as described by Zhu et al. (2022). GEOSCCM-fs also shows a similar initial plateau but with a larger magnitude of SWV mass compared to MLS in early 2022. A more pronounced decrease begins at the end of 2022, with the SWV mass eventually decreasing to a level comparable to MLS by early 2023. MIROC-CHASER-fs exhibits a larger initial water mass but with a shorter plateau, beginning its decrease by mid-2022, and decreasing to a comparable mass to MLS in early 2023. In contrast, MIROC-CHASER-fs-H_2O shows a similar initial mass and plateau to MLS, but with a slightly faster decrease at the end of 2023 compared to both MLS and MIROC-CHASER-fs. CMAM-

FS-H_2O shows a slightly larger initial SWV mass but displays a similar variation in 2023 and a comparable decreasing trend thereafter. Simulations from GSFC2D-GloSSAC, GSFC2D-OMPS, and GSFC2D-H_2O exhibit nearly identical SWV mass evolution, characterised by a shorter plateau and a more significant decline starting in mid-2022.

Background variability in the MLS observational record was calculated using 2-sigma interannual deviations over the 2005–2021 pre-Hunga period. When considering this variability, all modelled SWV mass anomalies fall within the two-standard-deviation range of the MLS data, indicating that the model simulations reasonably reproduce the observed evolution patterns. Additionally, the modelled SWV mass decrease slope in late 2023 is not as sharp as in early 2023, with a slight increase observed at the end of 2023 or early 2024 in models such as WACCM6MAM-CO, GEOSCCM-FS, and MIROC-CHASER-FS, although this increase is less pronounced compared to the one observed in MLS at the end of 2023.

Millán et al. (2024) estimated that the anomalous state induced by the Hunga eruption could diminish within 5–7 years based on an exponential decay using MLS observations—a timescale that closely aligns with projections from the model simulations in this study. Among the simulations, the only one with a coupled ocean (WACCM6MAM-CO) exhibits the shortest perturbation duration, with stratospheric H_2O mass returning to climatological levels within four years (by 2026). This may reflect faster transport and more efficient H_2O removal in the coupled ocean simulation compared to the fixed-SST configuration. Additional coupled-ocean simulations are needed to confirm this. The longest perturbation, lasting up to seven years (until 2029), is projected by MIROC-CHASER-FS, while the other models suggest a duration of approximately five years, until 2027. The current decreasing trend in MLS H_2O mass lies within the range of model projections, suggesting a potential perturbation lasting around five years. This prolonged anomaly has significant implications for the climate system.

The e-folding time of stratospheric H_2O mass is typically calculated from the initial injection; however, the HTHH-MOC protocol mandates a retained H_2O mass of approximately 150 Tg in January 2022. Due to variations in how models simulate the initial ice cloud formation and removal processes, the initial H_2O injection methods and magnitudes differ across models, as summarised in the second column of Table 2. The lowest initial injection occurs in WACCM6MAM-CO and WACCM6MAM-FS (150 Tg), whereas GEOSCCM-FS injects the highest amount (750 Tg). Given this disparity, calculating e-folding time from the initial injection would be inappropriate. Instead, we use the e-folding time from the peak H_2O mass as a more consistent metric for assessing H_2O lifetime.

The maximum H_2O mass across models generally falls within 130–160 Tg. Prior to initiating ensemble simulations, model adjustments were made to achieve the protocol target of 150 Tg retained by the end of January 2022. However, due to internal variability within free-running models, ensemble members exhibit different evolutionary trajectories, leading to variations in maximum H_2O burden among members (Figure S3.13). Additionally, differences in microphysical and dynamical processes across models further contribute to variations in both peak H_2O mass and timing of peak occurrence. WACCM6MAM-CO reaches its 136 Tg peak the fastest (within two months), whereas MIROC-CHASER-FS-H_2O takes the longest (ten months) to reach 148 Tg. The earliest e-folding time from peak mass occurs in November 2024 in GSFC2D-H_2O, while MIROC-CHASER-FS-H_2O exhibits the latest, in May 2026, with corresponding e-folding times of 31 and 43 months, respectively.

Interestingly, MIROC-CHASER-FS-H_2O reaches a lower peak mass and does so later than MIROC-CHASER-FS, yet both exhibit the same 43-month e-folding time. This suggests that co-injection of SO_2 with H_2O primarily influences the magnitude of H_2O mass in the early months—likely reducing ice cloud formation initially—but has limited impact on the long-term H_2O lifetime. In contrast, GSFC2D-H_2O shows no notable differences from GSFC2D-OMPS and GSFC2D-GloSSAC. Among all models, GSFC2D predicts the shortest e-folding time of 31 months from peak H_2O mass. This is similar to a global decay time with a lifetime of 30 months starting from July 2023 and assuming a constant first-order loss previously estimated from a H_2O-only GSFC2D simulation (Fleming et al., 2024). Using an offline 3D CTM, Zhou et al. (2024) projected an overall e-folding decay timescale of 48 months from July 2023. Notably, this timescale reflects removal of water vapour from the entire atmosphere, rather than from the stratosphere as considered here. As shown above, different quantities yield varying estimates of the H_2O mass lifetime. Therefore, it is crucial to specify which quantity is used when quantifying H_2O mass lifetime to ensure consistency and comparability across studies.

Water vapour distribution The observed MLS H_2O cloud (red inset box in Figure S3.14) experiences an initial subsidence phase, characterised by downward transport to approximately 40 hPa within the first few weeks, as also noted by Niemeier et al. (2023). This is followed by a stable phase, during which H_2O remains confined to the middle stratosphere, and a subsequent rising phase, where H_2O ascends into the upper stratosphere and gradually enters the lower mesosphere by the end of 2022. The initial subsidence and stable phases are attributed to the radiative cooling effects of H_2O injection (Niemeier et al., 2023), while the final rising phase—associated with strong upward transport—is linked to the Quasi-Biennial Oscillation (QBO) phase (Schoeberl et al., 2024). Beyond this phase, stratospheric water vapour transport is increasingly dominated by upward flux into the mesosphere above 1 hPa, resulting in a peak mesospheric burden of approximately 3–4 Tg by late 2023 (Figure S3.15). However, this mesospheric contribution represents only a small fraction of the total H_2O injected by the eruption (cf. Figures S3.15 and S3.12). The majority is progressively removed through stratosphere–troposphere exchange, particularly at high latitudes. For instance, in January 2025 (Figure S3.16a), a wedge-shaped region just above the tropopause marks a sharp decline in H_2O concentration, indicating a key region where much of the Hunga H_2O is removed from the stratosphere. Above this feature, high-latitude maxima in H_2O in both hemispheres are consistent with enhanced transport driven by the Brewer–Dobson circulation. This behaviour is further supported by evidence of pronounced dehydration in the Southern Hemisphere polar stratosphere during winter, as illustrated in July 2025 (Figure S3.16b), aligning with Antarctic vortex-induced dehydration mechanisms described by Zhou et al. (2024). These pathways are expected to continue dominating the removal of Hunga-injected H_2O as it is gradually transported downward by the global stratospheric circulation (Figure 10 in Randel et al., 2024). The anomalous H_2O distribution near 10 hPa is an artefact resulting from the placement of the MLS spectral channels (Niemeier et al., 2023).

The MLS anomaly is calculated relative to the 10-year climatology, and since the model anomalies are derived from Hunga eruption experiments relative to control runs without volcanic emissions, direct comparisons of detailed values are inappropriate. Therefore, our focus is on comparing the transport pattern. As shown in Figure S3.14, all models successfully reproduce the three-phase transport pattern. Among them, WACCM6MAM-FS, WACCM6MAM-CO, MIROC-CHASER-FS, and MIROC-CHASER-FS-H_2O exhibit slightly weaker upward transport, whereas GEOSCCM-FS, GSFC2D-GLOSSAC, GSFC2D-OMPS, and GSFC2D-H_2O show slightly stronger upward transport compared to MLS. However, the differences among GSFC2D-GLOSSAC, GSFC2D-OMPS, and GSFC2D-H_2O are quite small.

The three-phase transport pattern is also captured by the ICON-Seamless model in Niemeier et al. (2023), which simulated H_2O-only injection. That study highlighted that co-injection of SO_2 primarily affects the magnitude of vertical transport but does not alter the three-phase structure. This finding is further supported by comparisons between MIROC-CHASER-FS and MIROC-CHASER-FS-H_2O, as well as between GSFC2D-GLOSSAC, GSFC2D-OMPS, and GSFC2D-H_2O.

In the long term, significant H_2O anomalies in the stratosphere and lower mesosphere are projected to persist for at least six years, until 2028, in WACCM6MAM-CO. The longest projection indicates that a substantial anomaly could persist for over a decade, lasting until the end of the simulation in 2031, as indicated by MIROC-CHASER-FS and MIROC-CHASER-FS-H_2O. This prolonged anomaly may be attributed to weaker upward transport, particularly in MIROC-CHASER-FS-H_2O, as indicated by both the anomaly pattern and the position of the 1 ppmv H_2O contour line. The extended H_2O lifetime in MIROC-CHASER-FS-H_2O, as shown in Figure S3.11, further supports this conclusion.

S3.2.3 Global-mean air temperature evolution

The upper atmospheric global-mean air temperature anomaly calculated from MLS data indicates slight warming in the lower stratosphere during 2022, particularly in the first half of the year (Figure S3.17). Above this warming layer, strong cooling is observed in the middle and upper stratosphere, which extends into the lower mesosphere above 1 hPa from late 2022 onward.

The upper-level cooling and lower-level warming dipole response pattern is reasonably reproduced by the model simulations, although with a smaller magnitude in most models compared to MLS. The significant cooling in the middle stratosphere (10–40 hPa) is more persistent than in the upper stratosphere (1–10 hPa), lasting between 3.5 and 4.5 years—until mid-2025 in WACCM6MAM-co and mid-2026 in

GEOSCCM-FS. The strongest cooling is observed in the mesosphere above 1 hPa, where it persists for at least five years, until 2027, in GEOSCCM-FS and CMAM-FS-H_2O. This cooling persists even longer in simulations by WACCM6MAM, MIROC-CHASER, and GSFC2D, with the longest duration—up to 10 years—observed in MIROC-CHASER-FS-H_2O. The modelled significant warming in the lower stratosphere is most prominent in 2022 in GEOSCCM-FS and MIROC-CHASER-FS. However, a more prolonged warming, extending into early and mid-2023, is observed in WACCM6MAM-CO and WACCM6MAM-FS. This warming is also evident—and even stronger—in GSFC2D-GloSSAC and GSFC2D-OMPS.

The cooling observed in the middle and upper stratosphere corresponds to the ascent of H_2O, while the warming in the lower stratosphere is associated with the descent of aerosols that absorb solar near-infrared and terrestrial infrared radiation (Wang et al., 2023). Compared to MIROC-CHASER-FS, MIROC-CHASER-FS-H_2O exhibits stronger and more prolonged cooling in the middle stratosphere but less pronounced warming in the lower stratosphere. A similar pattern is observed when comparing GSFC2D-H_2O with GSFC2D-GloSSAC and GSFC2D-OMPS, where the former shows enhanced middle stratosphere cooling but weaker lower stratosphere warming. Although the greenhouse effect of stratospheric H_2O contributes to lower stratospheric warming, the significant warming is primarily driven by the co-injection of aerosols.

S3.2.4 Global-mean ozone variation

MLS data indicate ozone depletion in the lower stratosphere (20–100 hPa), an ozone increase in the middle stratosphere (around 10 hPa), and ozone depletion in the upper stratosphere (1–5 hPa), with the most pronounced depletion occurring in the lower mesosphere (0.1–1 hPa) during mid-2023 to 2024 (Figure S3.18). This triple-response pattern—characterised by middle-stratospheric ozone enhancement flanked by depletion above and below—is well captured by all model simulations, except for CMAM-FS-H_2O, which exhibits very limited ozone depletion in the lower stratosphere. However, the magnitude and timing of these ozone changes vary among models.

All simulations project long-lasting ozone depletion in the lower mesosphere, persisting for at least seven years. MIROC-CHASER-FS shows the most prolonged ozone depletion, extending to the end of the simulation (December 2031), and also exhibits the most pronounced ozone increase in the middle stratosphere, as well as extended significant ozone depletion in the lower stratosphere between 2022 and 2025.

Compared to MIROC-CHASER-FS, MIROC-CHASER-FS-H_2O shows a smaller ozone increase in the middle stratosphere and less ozone depletion in the lower stratosphere. The significant ozone depletion between 20 and 40 hPa observed in GSFC2D-GloSSAC and GSFC2D-OMPS in 2022 is less pronounced in GSFC2D-H_2O. This highlights the crucial role of co-injected SO_2 in driving ozone depletion in the lower stratosphere. These findings confirm the combined effect of both H_2O and SO_2, as discussed by Wang et al. (2023).

Ozone depletion in the lower stratosphere is driven by heterogeneous chlorine activation and enhanced dinitrogen pentoxide on hydrated aerosols (Evan et al., 2023; Zhang et al., 2024; Zhu et al., 2022; Zhu et al., 2023). In contrast, ozone depletion in the lower mesosphere is linked to increased reactive hydrogen and a corresponding reduction in equilibrium ozone (Fleming et al., 2024; Randel et al., 2024), resulting from the upward transport of water vapour (Figure S3.14) that leads to significant cooling (Figure S3.17). The depleted ozone layer absorbs less ultraviolet (UV) radiation, further amplifying cooling at these altitudes. Consequently, stronger UV radiation enhances ozone production in the middle stratosphere, while ozone concentrations decrease above this layer.

Furthermore, direct chemical effects contribute to increased ozone in the mid-stratosphere. These include the heterogeneous reaction

$$N_2O_5 + H_2O \rightarrow 2 \times HNO_3$$

on enhanced sulfate aerosols, which reduces NO_x and the odd-nitrogen ozone loss cycle at altitudes where aerosols are abundant (Wilmouth et al., 2023; Santee et al., 2023; Zhang et al., 2024). The enhanced OH from the H_2O injection converts NO_2 to the reservoir HNO_3, also reducing the odd-nitrogen ozone loss cycle in the mid-stratosphere (Fleming et al., 2024). Beyond the chemical feedback effects, the increase in ozone in the middle stratosphere is also influenced by transport changes associated with a weakening of the midlatitude Brewer–Dobson circulation (Wang et al., 2023).

The ozone response mechanisms discussed here draw on previous single-model studies that conducted detailed photochemical analyses using the same modelling frameworks. While the current study does not include new quantitative calculations of individual reaction rates or radiative effects, a dedicated multi-model analysis of the ozone response and its underlying mechanisms is currently underway.

S3.2.5 Summary and conclusions

The 2022 Hunga eruption was the most explosive volcanic event since the 1991 Pinatubo eruption. In contrast to Pinatubo, which injected a large amount of SO_2, Hunga released only approximately 0.5 Tg of SO_2 but was distinguished by an unprecedented injection of roughly 150 Tg of water vapour into the stratosphere, with some reaching the lower mesosphere. To investigate the evolution of SO_2 and H_2O perturbations and their subsequent atmospheric and climate impacts, the HTHH-MOC activity was endorsed by the WCRP APARC, fostering collaboration between the observational and modelling communities. In this study, we evaluate multi-model simulations against observations for the first two years, along with subsequent projections of their evolution, using Experiment 1—the only long-term simulation extending up to 10 post-eruption years. This assessment aims to evaluate model reliability in capturing the evolution of volcanic emissions and predicting their impacts on temperature and ozone in the stratosphere and lower mesosphere.

Our results indicate that models successfully reproduce the latitudinal distribution of aerosols, which initially exhibit southward transport in the first year and reach Southern Hemisphere (SH) polar latitudes by the austral winter of 2023, reflecting stratospheric transport dominated by the Brewer–Dobson circulation. Aerosols persist for approximately two years, with some models suggesting an additional 0.5 to 1.5 years of persistence in polar latitudes.

MLS observations show a plateau in H_2O mass between 1 and 70 hPa during the first year, followed by a continuous decline starting in late 2022. Models generally reproduce this plateau in 2022, with a subsequent sharp decline beginning in 2023. However, MIROC-CHASER-FS deviates by showing a shorter plateau, with a continuous decrease starting from mid-2022. The significant H_2O perturbation is projected to last four years (until 2026) in WACCM6MAM-CO and seven years (until 2029) in MIROC-CHASER-FS. The impact of this 4–7 year stratospheric water vapour perturbation on stratospheric and lower mesospheric chemistry and dynamics remains an open question and requires further investigation. Understanding these effects is crucial for improving climate change detection and attribution in the coming years.

To comply with the experiment protocol, different models simulated H_2O injection using various methods and initial injection amounts, ranging from 150 Tg in WACCM6MAM-CO and WACCM6MAM-FS to 750 Tg in GEOSCCM-FS. This variation in injection amounts results in differences in the maximum H_2O mass across models, which range from 139 Tg in WACCM6MAM-FS to 166 Tg in GSFC2D-H_2O. The e-folding time is calculated based on the maximum mass rather than the initial injection amount, given the substantial differences in initial injection sizes. The estimated e-folding times range from 31 months in GSFC2D-H_2O to 43 months in MIROC-CHASER-FS and MIROC-CHASER-FS-H_2O.

Both observations and model simulations indicate warming in the lower stratosphere and significant cooling above, accompanied by ozone depletion in the lower stratosphere, an ozone increase in the middle stratosphere, and severe ozone depletion in the upper stratosphere and lower mesosphere. The ozone depletion persists for at least seven years, with some model projections extending up to at least a decade. Comparisons between simulations with combined SO_2 and H_2O injection and those with H_2O-only injection reveal that the significant cooling and ozone depletion in the upper stratosphere and lower mesosphere result from the presence of excessive water vapour. Additionally, the co-injection of SO_2 with H_2O is necessary to reproduce the significant warming and ozone depletion in the lower stratosphere, albeit with a limited amount of SO_2 injection.

In conclusion, the models effectively reproduce the overall transport patterns of SO_2 and H_2O, with varying lifetimes projected across different models. They also reproduce the observed patterns of temperature and ozone variations following the eruption, albeit with differences in timescales and magnitudes. As the first study to utilise multi-model simulations of the Hunga eruption, this research provides valuable insights into the long-term evolution of Hunga-injected water vapour and aerosols, as well as their impacts on stratospheric temperatures and ozone. Furthermore, this study demonstrates the reliability of these model simulations in assessing the underlying physical and dynamical mechanisms and their potential atmospheric and climate impacts in the coming years.

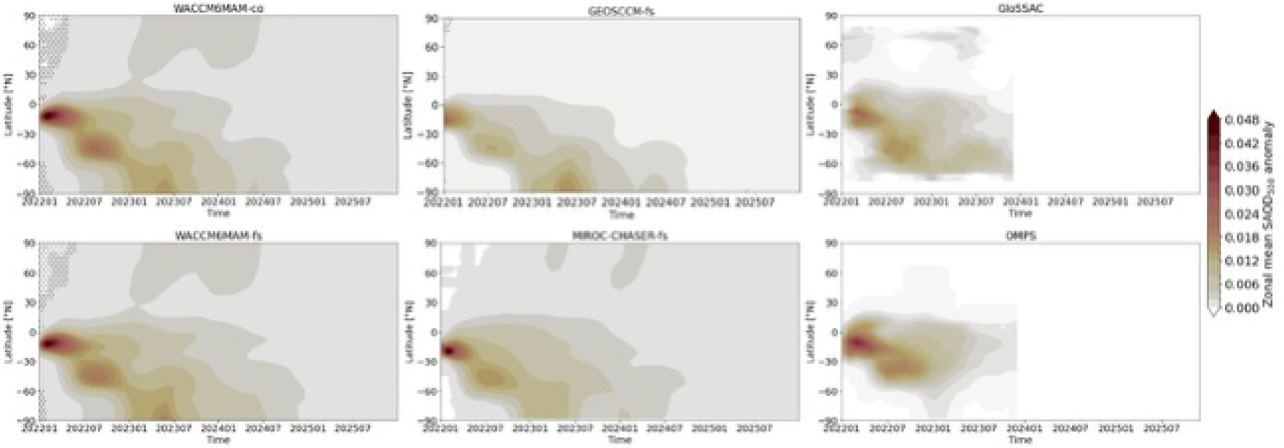

Figure S3.11: *Hovmöller diagrams of global mean stratospheric aerosol optical depth (SAOD) anomalies following the Hunga eruption. The four left panels present ensemble mean anomalies from different models relative to the control run, with dotted areas indicating statistically insignificant anomalies at the 95% confidence level based on Student's* t*-tests. The top-right panel shows the observed anomaly from the Global Space-based Stratospheric Aerosol Climatology (GloSSAC), relative to the 2012–2021 climatological period. The aerosol extinction of the GloSSAC data was used in the GSFC2D model as their prescribed aerosol field input (Zhu et al., 2025). The bottom-right panel displays the Stratospheric Aerosol Optical Depth (SAOD) calculated from aerosol extinction data obtained from the Ozone Monitoring and Profiler Suite Limb Profiler (OMPS), which was utilised in the GSFC2D model.*

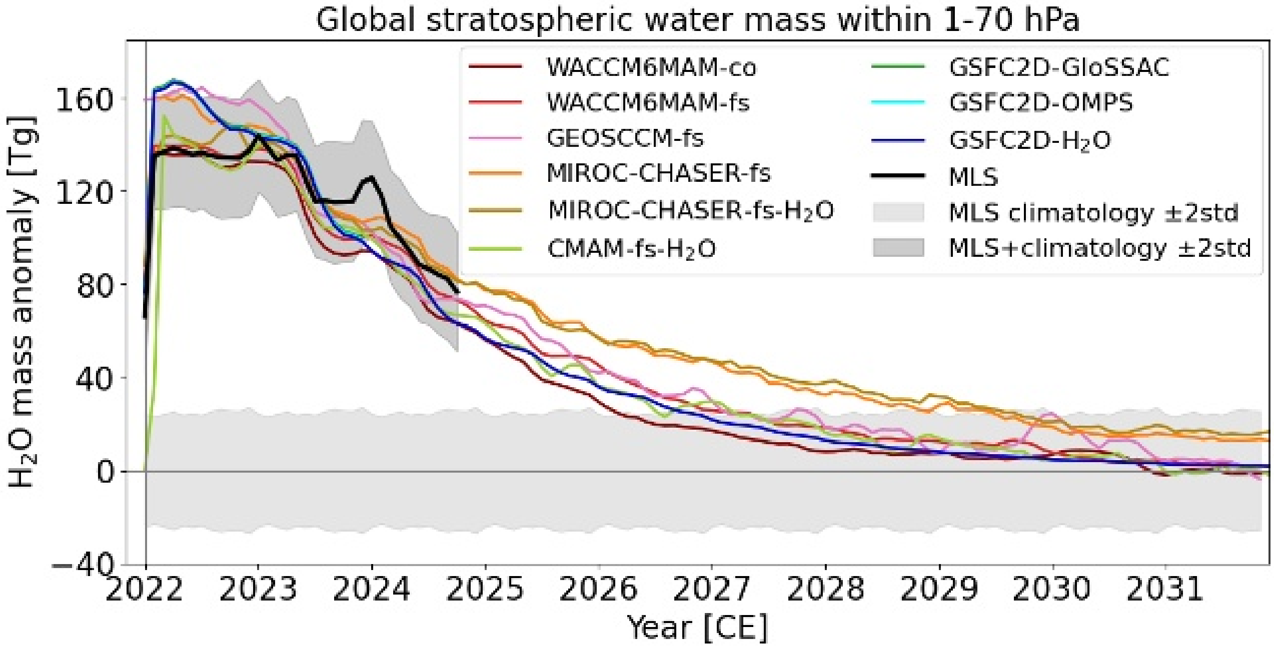

Figure S3.12: *Simulated and observed global stratospheric H_2O mass anomalies within the 1–70 hPa range following the Hunga eruption. The coloured lines represent ensemble mean anomalies relative to the control run, while the black line and grey shading depict the observed anomaly from the Microwave Limb Sounder (MLS) water vapour mass, along with its ±2 standard deviation range from the 2012–2021 climatology period. GSFC2D-GloSSAC and GSFC2D-OMPS have only two years of simulations and are superseded by GSFC2D-H_2O with ten years of simulations.*

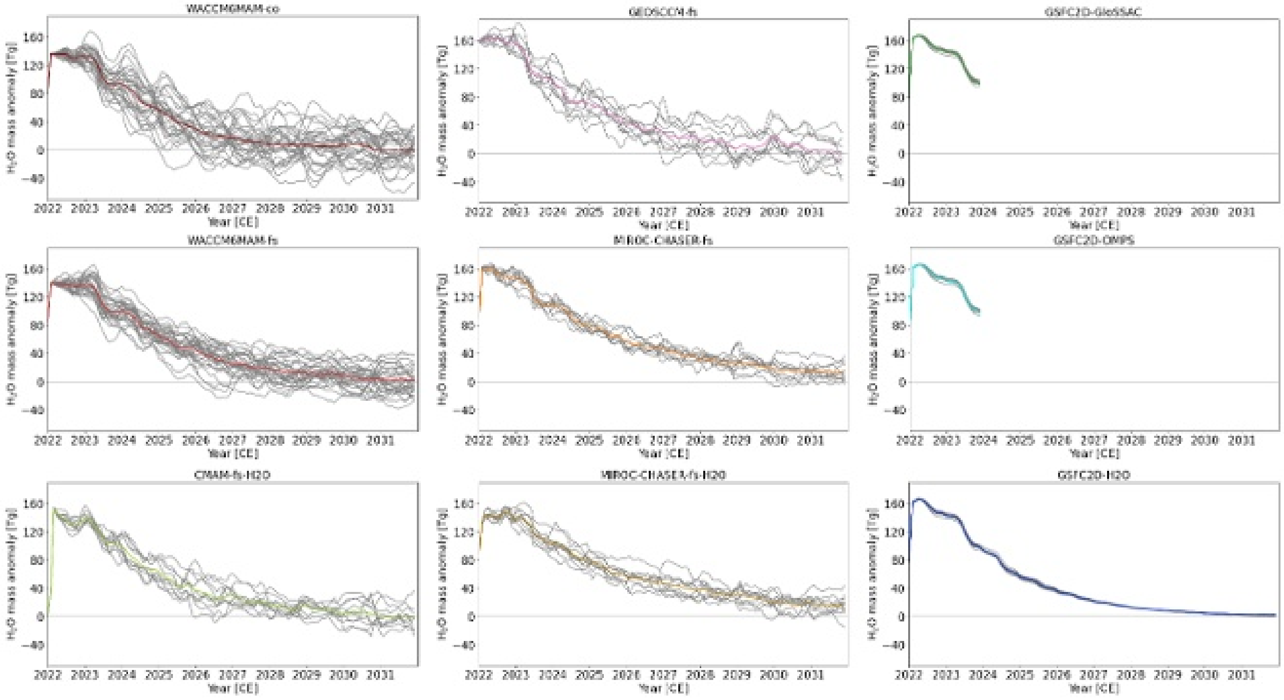

Figure S3.13: *Simulated global stratospheric H_2O mass anomalies within the 1–70 hPa range following the Hunga eruption. Coloured lines represent ensemble mean anomalies relative to the control run, while grey lines indicate individual ensemble member anomalies.*

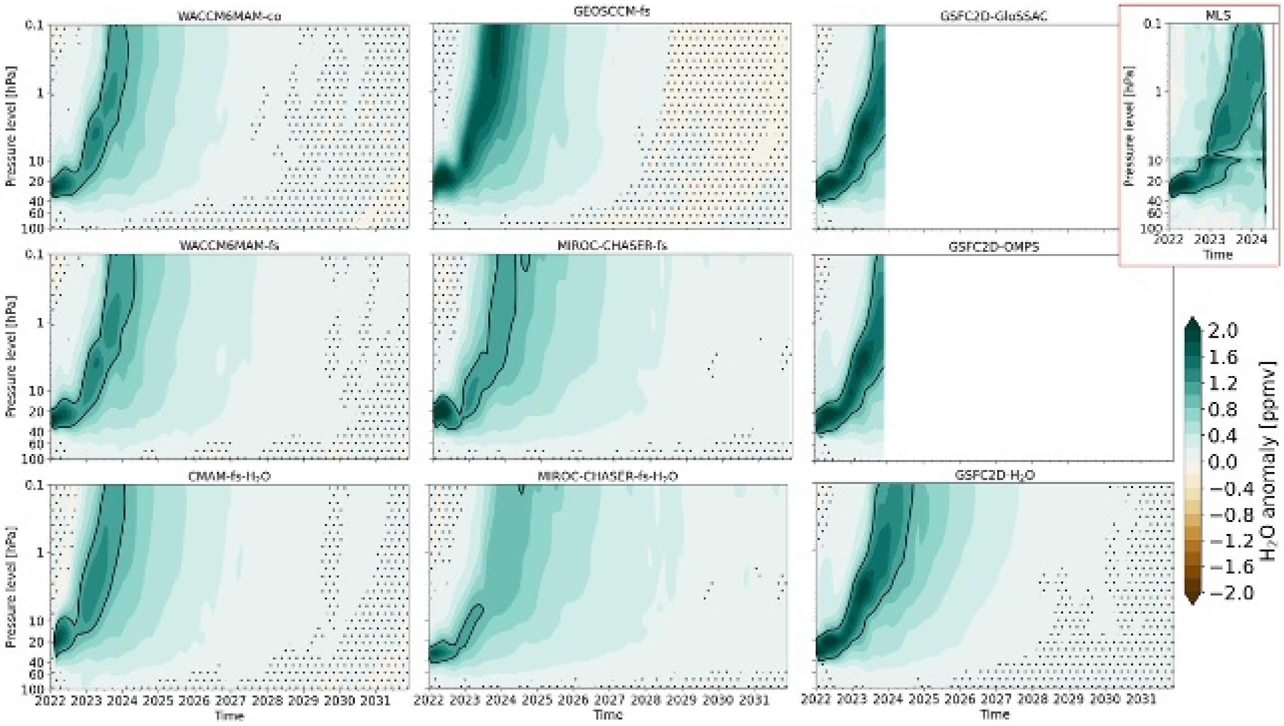

Figure S3.14: *Simulated and observed (red inset box) global mean H_2O anomalies following the Hunga eruption. The modelled anomalies are relative to the control run. Dotted grids indicate statistically insignificant anomalies at the 95% confidence level based on Student's t-tests. The solid black contours indicate an anomalous H_2O concentration of 1 ppmv.*

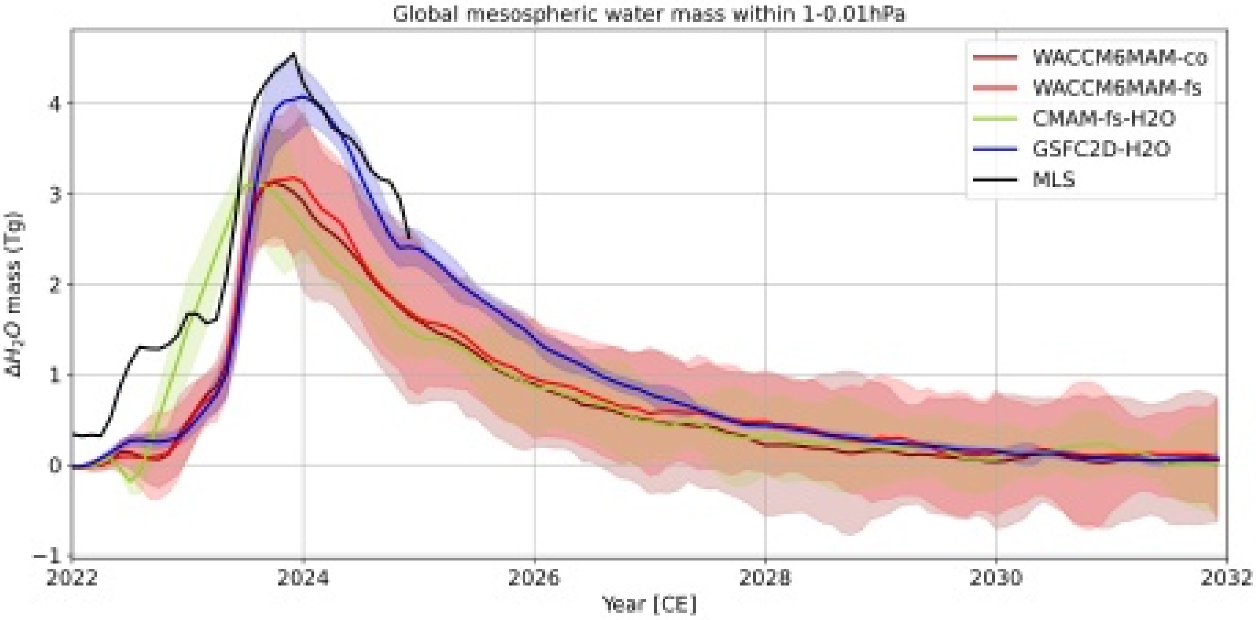

Figure S3.15: *Simulated and observed global stratospheric H_2O mass anomalies within the 1–0.01 hPa pressure range following the Hunga eruption. Coloured lines show ensemble mean anomalies relative to the control simulations for each model, with shading indicating the respective ensemble spreads. The black line represents the observed anomaly derived from Microwave Limb Sounder (MLS) water vapour measurements.*

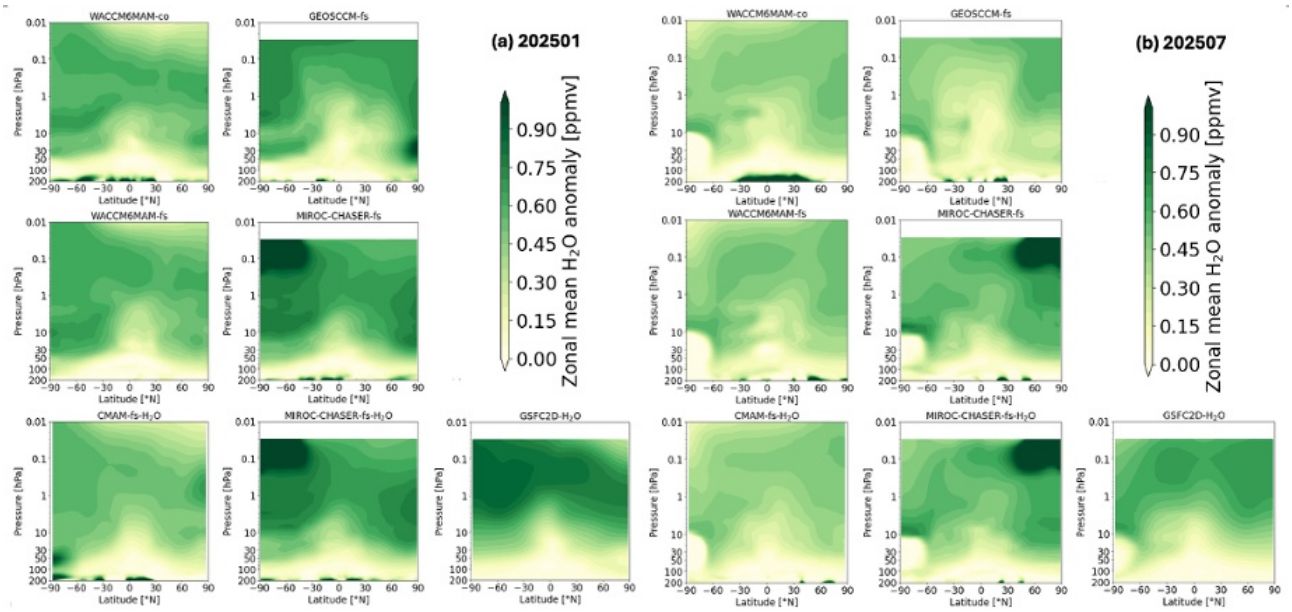

Figure S3.16: *Latitude–pressure distribution of simulated zonal mean water vapour anomalies in the upper atmosphere following the Hunga eruption, shown for (a) January 2025 and (b) July 2025. Anomalies are computed as differences between the ensemble mean of the experiment and control simulations.*

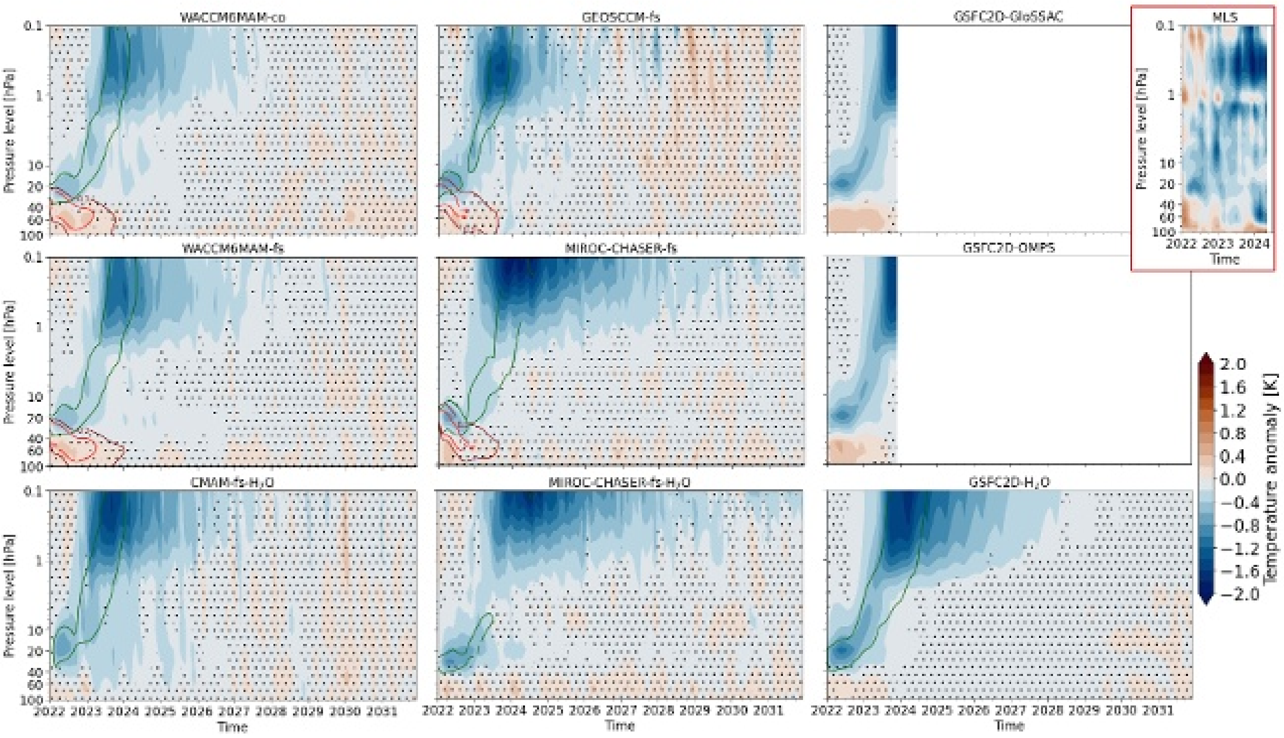

Figure S3.17: *Simulated and observed (red inset box) global mean air temperature anomalies following the Hunga eruption. The modelled anomalies are relative to the control run. Dotted grids indicate statistically insignificant anomalies at the 95% confidence level based on Student's* t*-tests. Dark red and red contour lines denote modelled aerosol extinction coefficients at 0.3 and 0.6×10^{-3} km^{-1}, respectively, while dark green contour lines indicate modelled water vapour concentrations of 1 ppmv.*

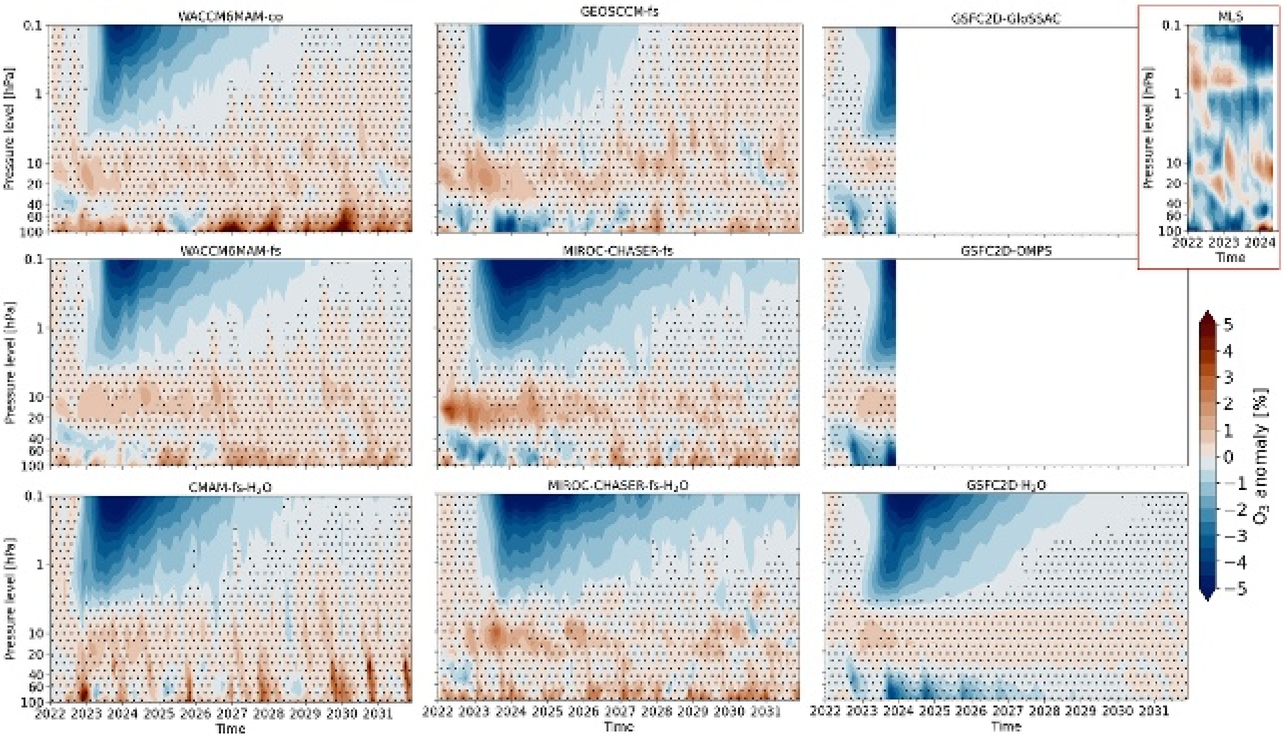

Figure S3.18: *Simulated and observed (red inset box) global mean ozone anomalies following the Hunga eruption. The modelled anomalies are relative to the control run. Dotted grids indicate statistically insignificant anomalies at the 95% confidence level based on Student's* t*-tests.*

S3.3 Hunga impact on radiative forcing

Authors Ilaria Quaglia
Daniele Visioni
Ewa M. Bednarz
Yunqian Zhu
Georgiy Stenchikov
Valentina Aquila
Cheng-Cheng Liu
Graham W. Mann
Yifeng Peng
Takashi Sekiya
Simone Tilmes
Xinyue Wang
Shingo Watanabe
Pengfei Yu
Jun Zhang
Zhihong Zhuo
Wandi Yu

This section is based on: Quaglia et al. (2025).

Quaglia, I., Visioni, D., Bednarz, E. M., Zhu, Y., Stenchikov, G., Aquila, V., Liu, C.-C., Mann, G. W., Peng, Y., Sekiya, T., Tilmes, S., Wang, X., Watanabe, S., Yu, P., Zhang, J., and Yu, W.: Multi-model analysis of the radiative impacts of the 2022 Hunga eruption indicates a significant cooling contribution from the volcanic plume, *EGUsphere [preprint]*, `https://doi.org/10.5194/egusphere-2025-3769`, 2025.

This section presents an inter-model comparison using both Exp1 and Exp2 results to quantify the direct radiative forcing contributions of aerosols and water vapour perturbations following the Hunga eruption.

Chapter 7: methodology – radiative forcing calculation

Instantaneous Radiative Forcing (IRF) is computed as the difference between the perturbed and unperturbed cases, using simulations with nudged meteorological fields (Exp2a, hereafter "Nudged"). The IRF of combined sulfate aerosols and water vapour, as well as of each component separately, is derived from the nudged experiments SO_2andH_2O, SO_2only, and H_2Oonly, respectively.

The Effective Radiative Forcing (ERF) and Radiative Forcing (RF) are calculated analogously to the IRF, but based on free-running simulations with either fixed sea surface temperatures (SSTs) or coupled ocean configurations: Exp1_fixedSST (here "Fixed SST") and Exp1_coupled (here "Coupled"). In figure titles and captions, these cases are collectively referred to simply as *radiative forcing*.

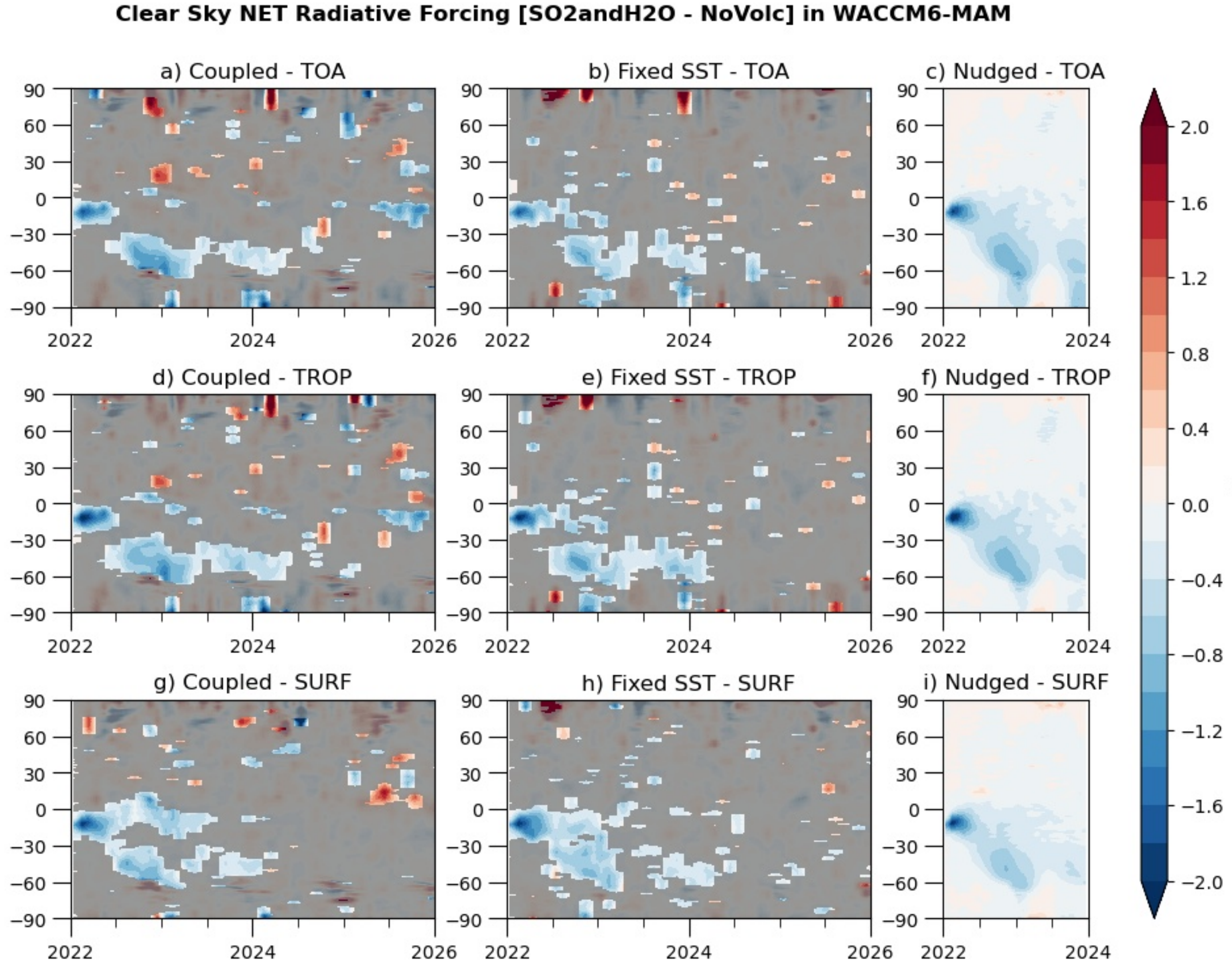

Figure S3.19: *Time series of zonal mean radiative forcing under clear-sky conditions for the SO_2ANDH$_2$O experiment in WACCM6-MAM, at (a–c) the top of the atmosphere (TOA), (d–f) the tropopause (TROP), and (g–i) the surface (SURF). Each column represents a different model setup: first column shows nudged simulations (Exp2a), second column fixed sea surface temperature simulations (Exp1–Fixed SST), third column coupled ocean simulations (Exp1–Coupled). Results from Exp1–Fixed SST and Exp1–Coupled are ensemble means. Gray areas indicate regions where the differences are not statistically significant at the 5% level based on Student's* t*-test.*

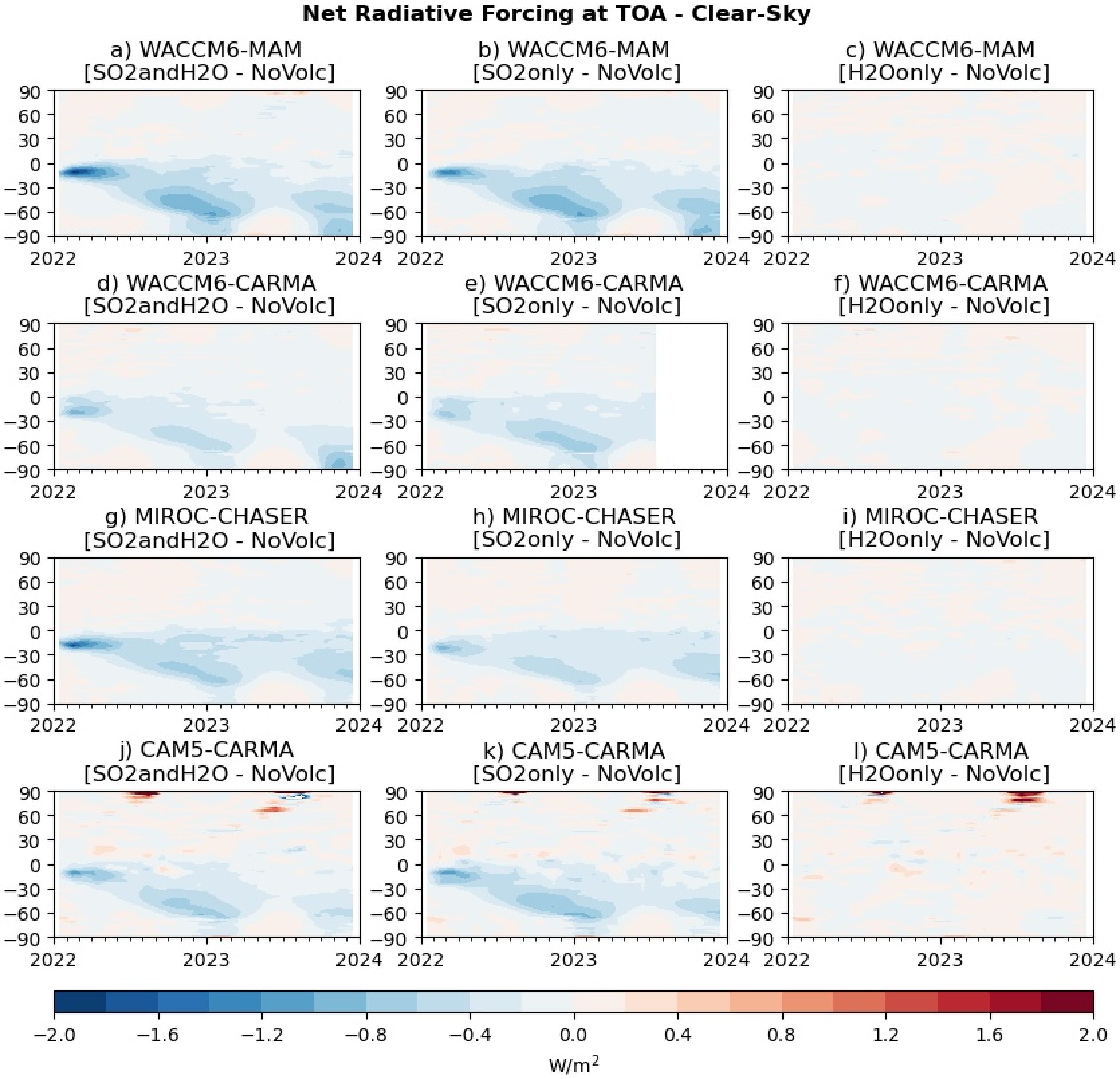

Figure S3.20: *Time series of zonal mean radiative forcing at the top of the atmosphere (TOA) under clear-sky conditions from five models: WACCM6-MAM (a–c), WACCM6/CARMA (d–f), MIROC-CHASER (g–i), and CAM5/CARMA (j–l). Each column corresponds to a different perturbation scenario from the nudged experiment (Exp2a): the first column shows SO_2ANDH$_2$O, the second SO_2ONLY, and the third H_2OONLY.*

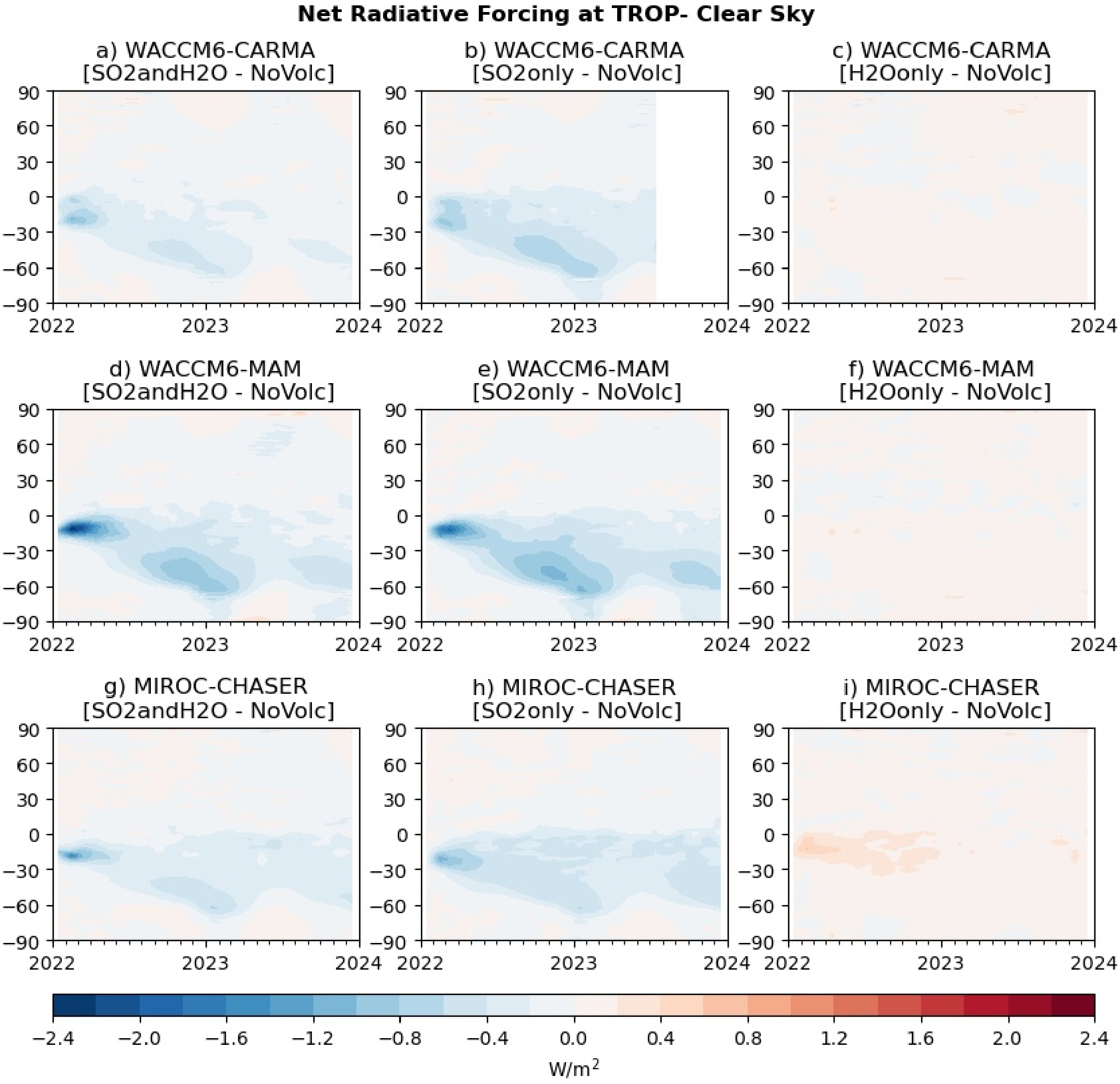

Figure S3.21: *As in Figure S3.20, but showing radiative forcing at the tropopause (TROP).*

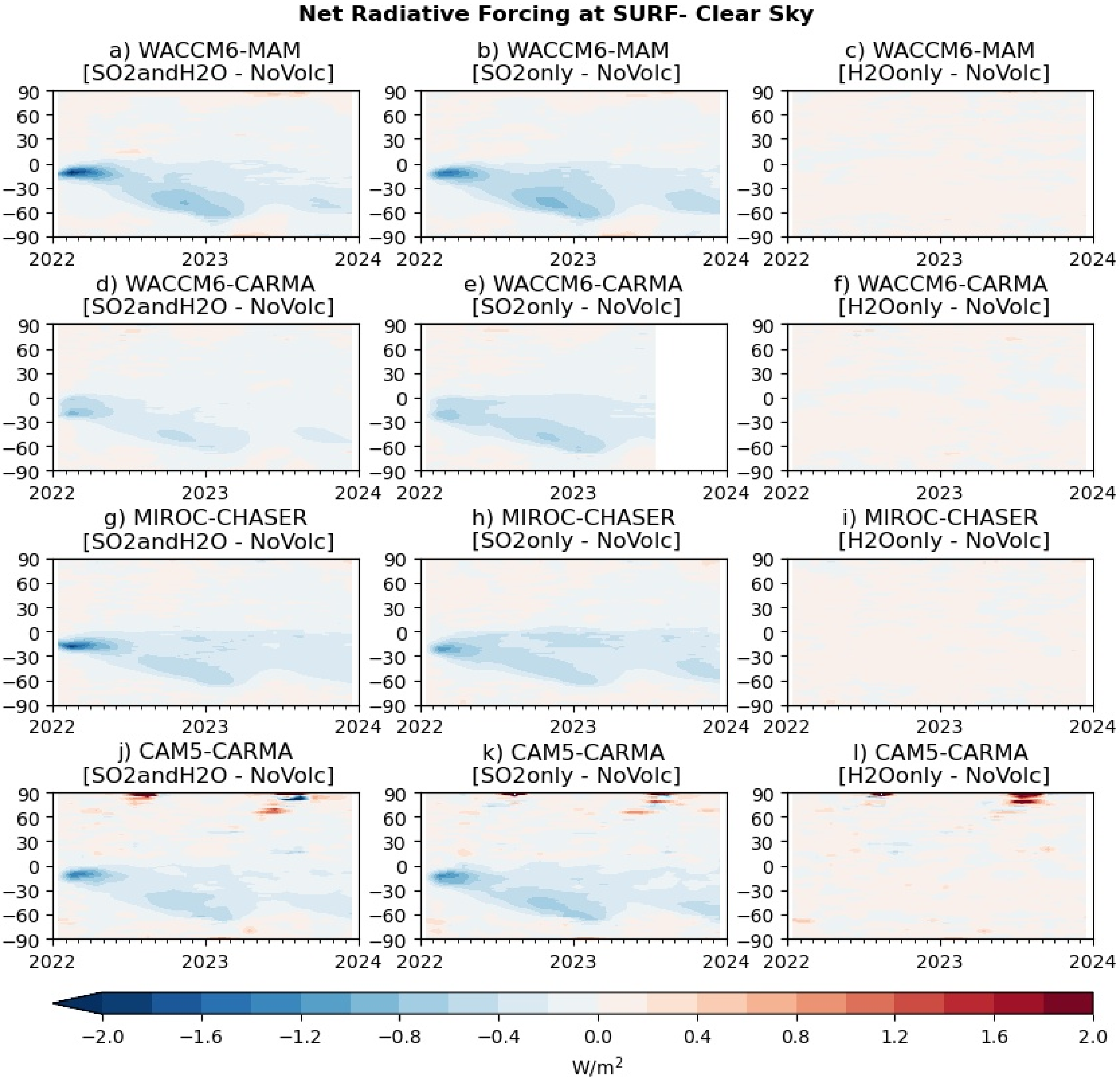

Figure S3.22: *As in figure S3.20, but showing radiative forcing at the surface (SURF).*

S3.4 Indirect climate impacts of the Hunga eruption

Authors Ewa M. Bednarz
Amy H. Butler
Xinyue Wang
Zhihong Zhuo
Wandi Yu
Georgiy Stenchikov
Matthew Toohey
Yunqian Zhu

This section is based on: Bednarz et al. (2025b).

Bednarz, E. M., Butler, A. H., Wang, X., Zhuo, Z., Yu, W., Stenchikov, G., Toohey, M., and Zhu, Y.: Indirect climate impacts of the Hunga eruption, *EGUsphere [preprint]*, `https://doi.org/10.5194/egusphere-2025-1970`, 2025.

Using two 30-member WACCM6MAM Exp1 ensembles run with either fixed SSTs/sea-ice (HUNGA_fix) or coupled ocean configuration (HUNGA_cpl).

S3.4.1 Simulated changes in near-surface air temperatures following the eruption

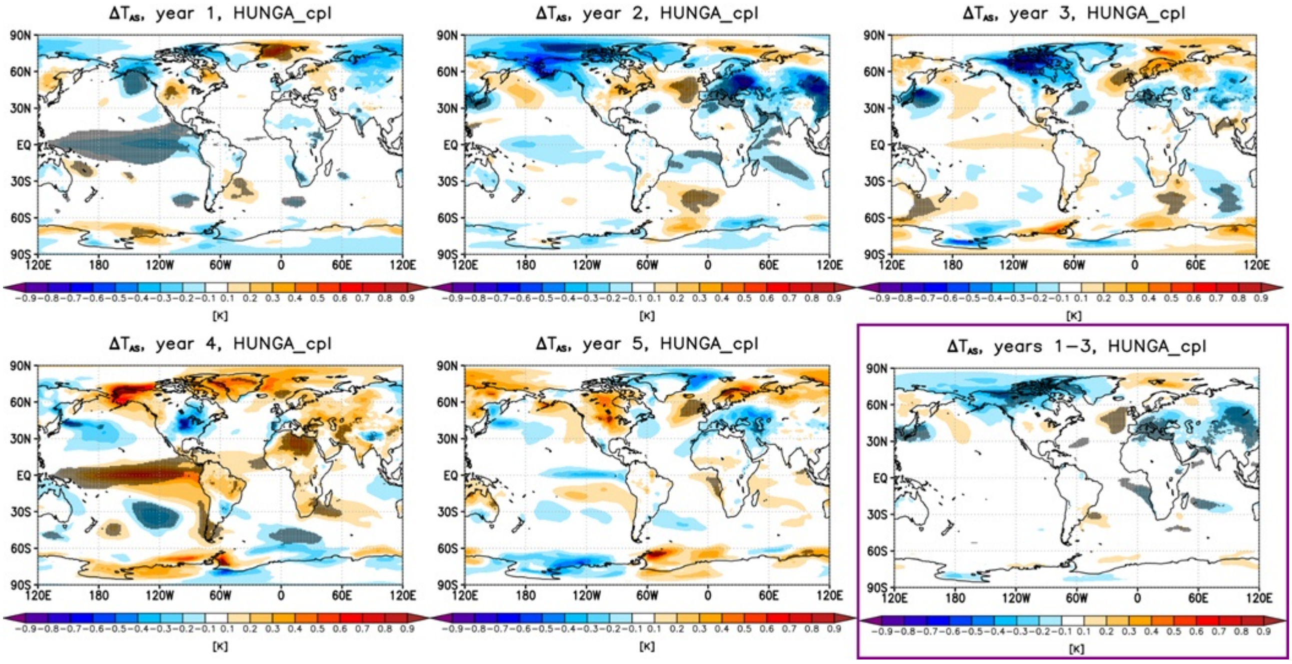

Figure S3.23: *Yearly mean changes in near-surface air temperature between the forced simulation and the control in the coupled ocean simulations for each of the five years following the eruption (2022–2027). The bottom right panel shows the response averaged over the first three years (2022–2024). Stippling indicates statistical significance, defined as differences exceeding ±2 standard errors in the difference of means.*

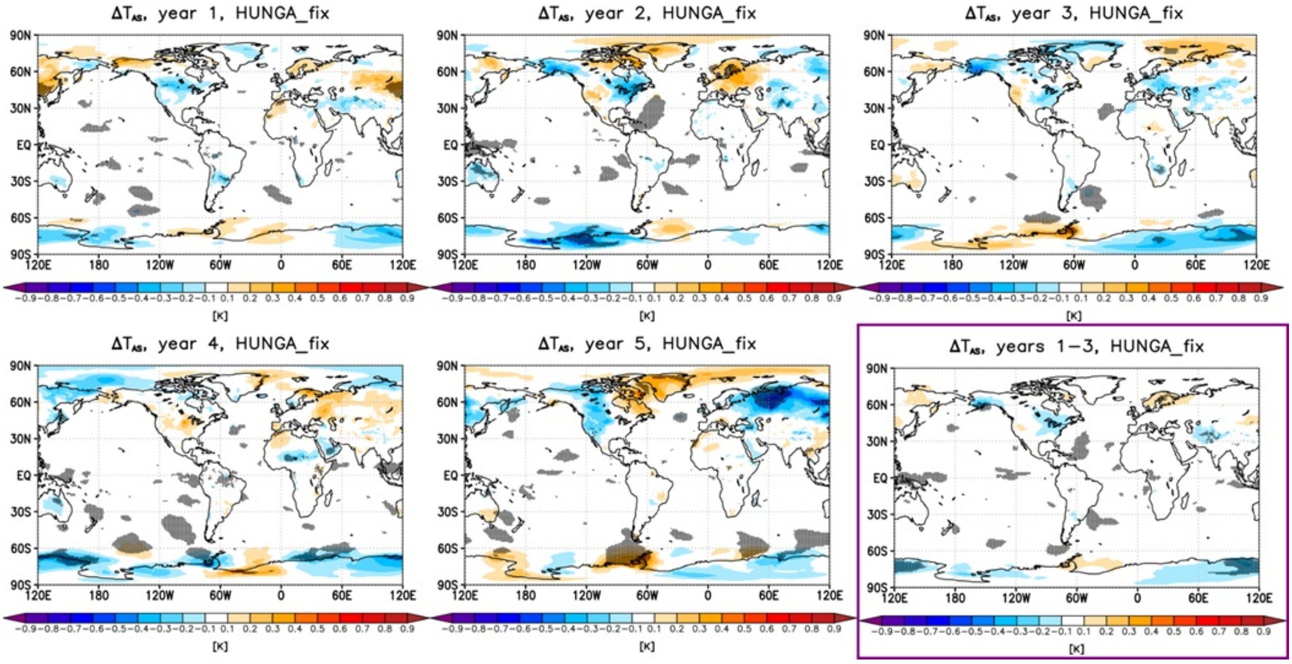

Figure S3.24: *As in Figure S3.23, but for the changes in the atmosphere-only simulations.*

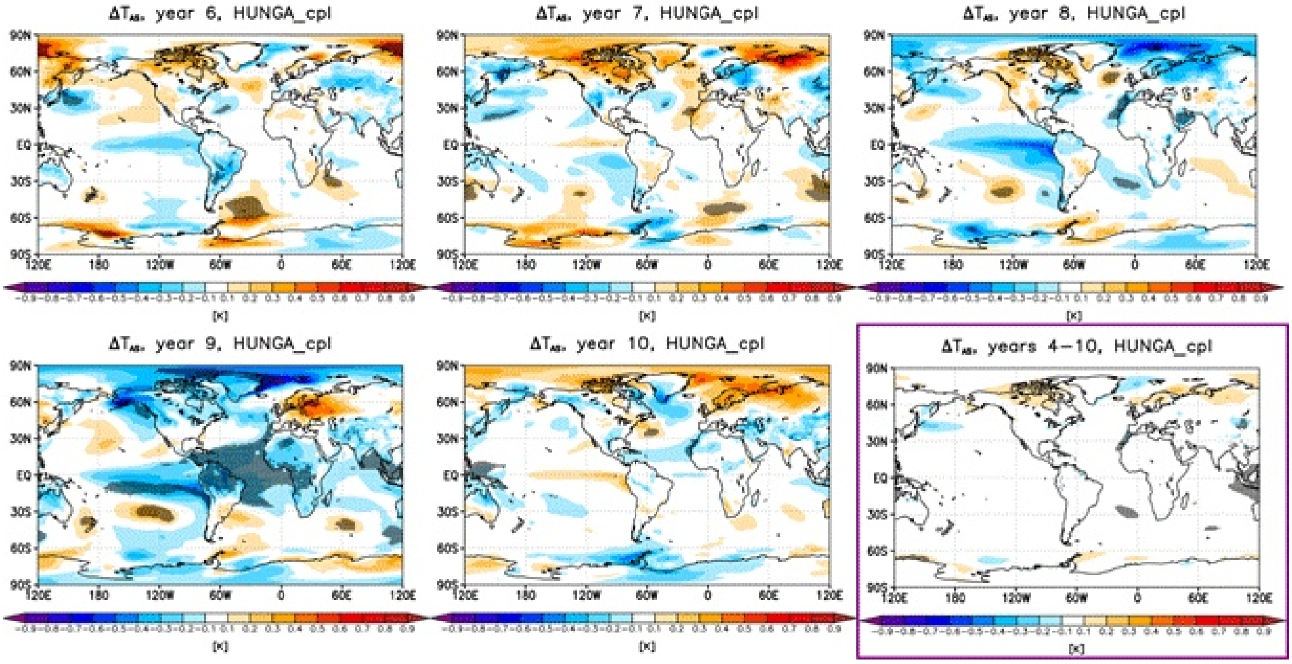

Figure S3.25: *As in figure S3.23, but for years 5–10.*

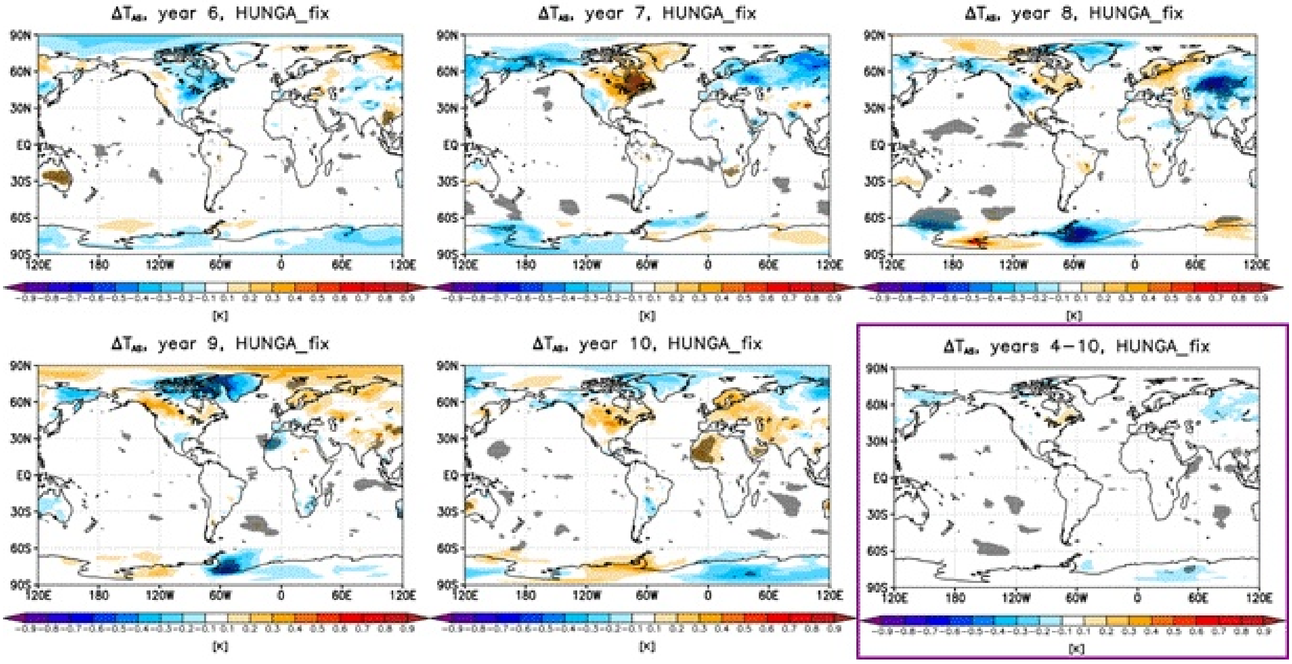

Figure S3.26: *As in Figure S3.24, but for years 5–10.*

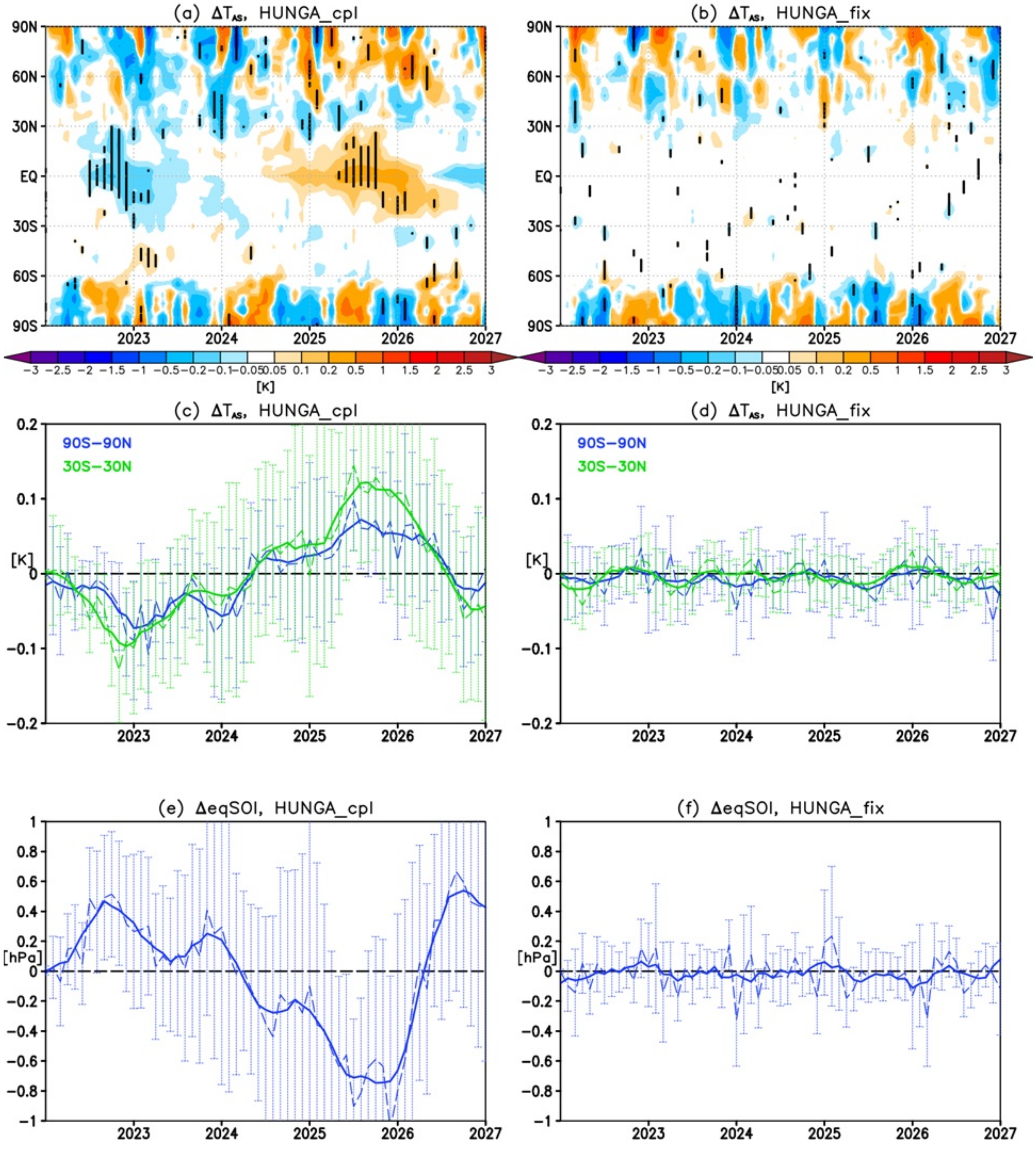

Figure S3.27: *Time series of changes in (a–b) zonal mean near-surface air temperature, (c–d) global and tropical mean near-surface air temperature, and (e–f) the eqSOI index between the forced simulation and the control in the coupled ocean (left) and atmosphere-only (right) simulations. Dashed lines in panels (c–f) indicate ensemble mean changes and solid lines their five-month running means. Error bars in panels (c–f) denote confidence intervals of the ensemble mean changes (±2 standard errors).*

S3.4.2 Seasonal changes in the NH polar vortex and impacts on the extratropical surface climate

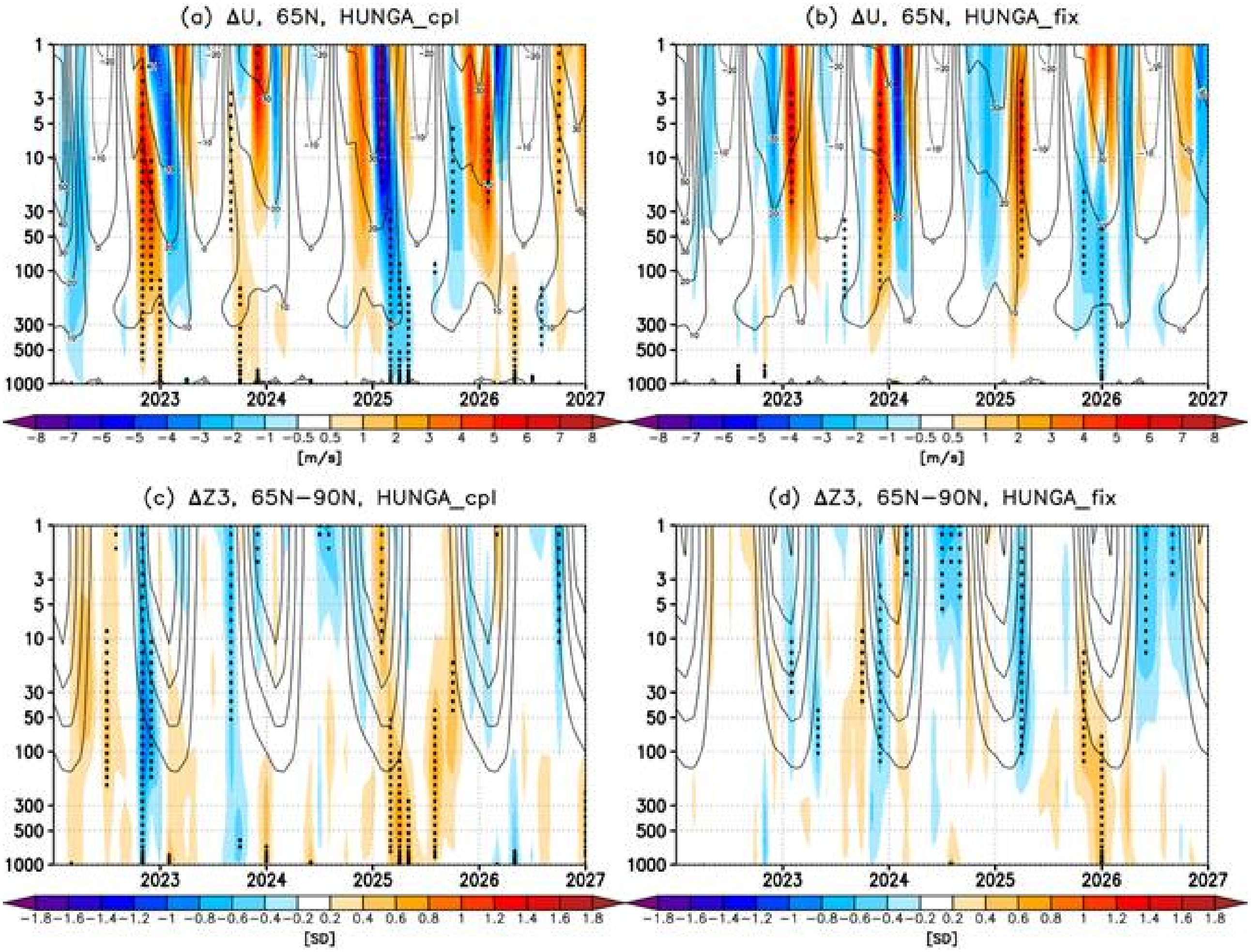

Figure S3.28: *Evolution of the Northern Hemisphere (NH) polar vortex. Shading: time series of ensemble-mean changes in (a–b) zonal wind at 65°N (in m s^{-1}) and (c–d) geopotential height (in standard deviations) averaged over the polar cap (65°–90°N) between the forced simulation and the control. Left panels correspond to the coupled ocean simulations, right panels to the atmosphere-only simulations. Stippling denotes statistical significance (defined as in Figure S3.23). Contours indicate values in the control for reference.*

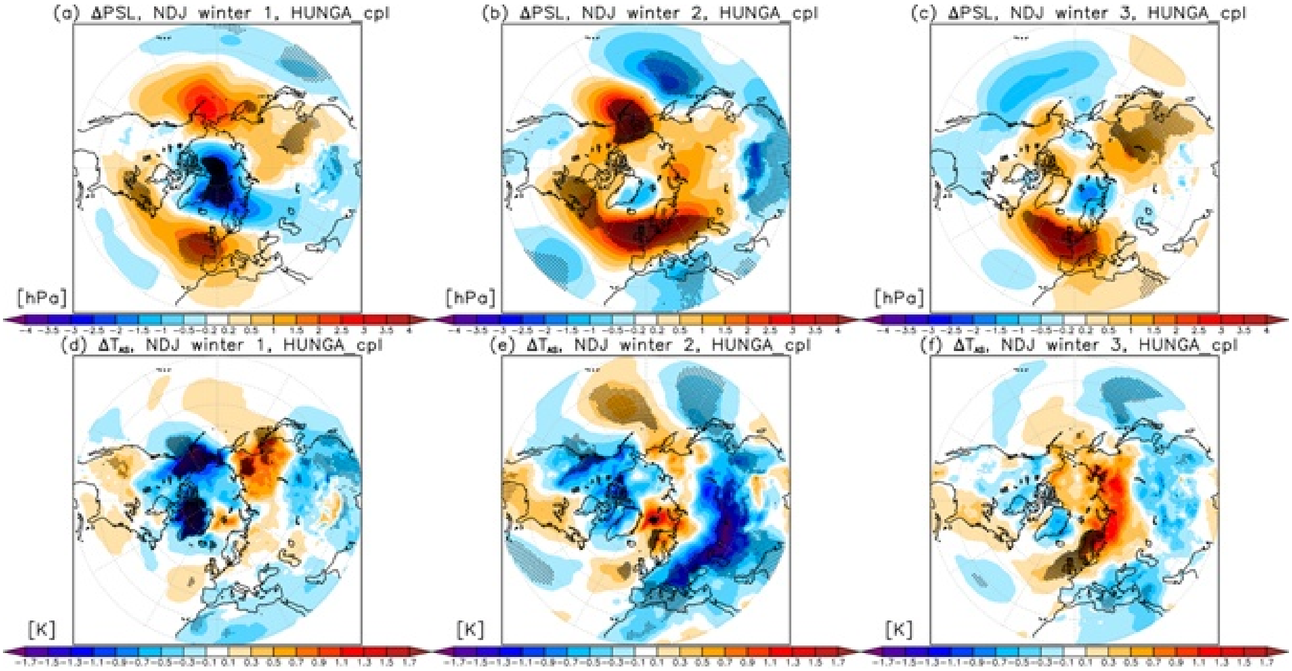

Figure S3.29: *Changes in early NH winter (November–December–January) ensemble-mean (top) sea-level pressure and (bottom) near-surface air temperature between the forced simulation and the control in the coupled ocean simulations for the first (2022/2023), second (2023/2024), and third (2024/2025) winters following the eruption (columns). Stippling denotes statistical significance (defined as in Figure S3.23).*

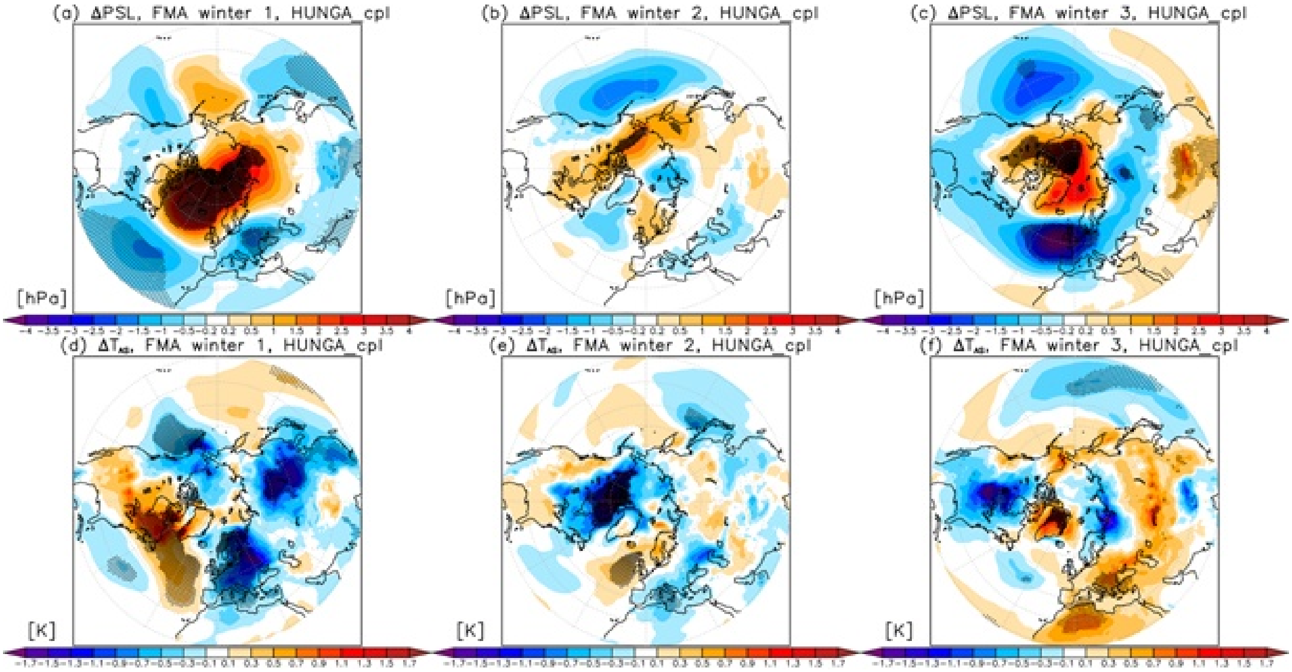

Figure S3.30: *As in Figure S3.29, but for the corresponding late NH winter (February–March–April) changes.*

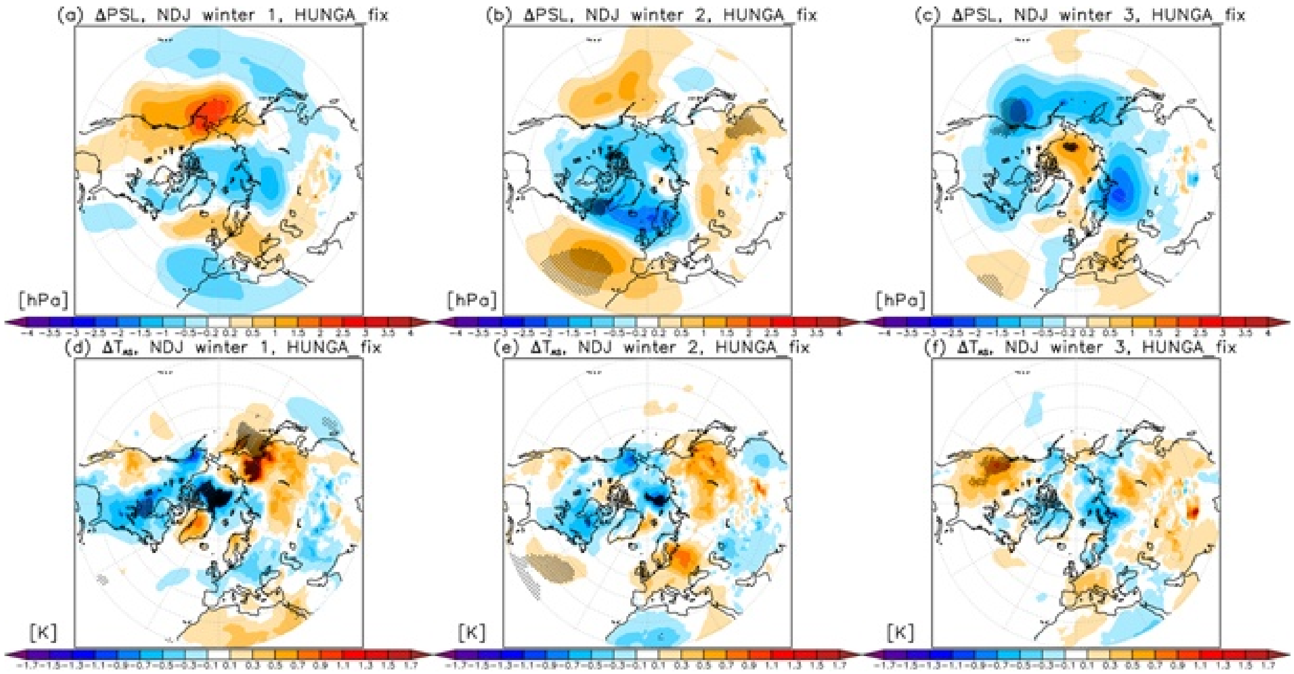

Figure S3.31: *As in Figure S3.29, but for the changes in the atmosphere-only simulations.*

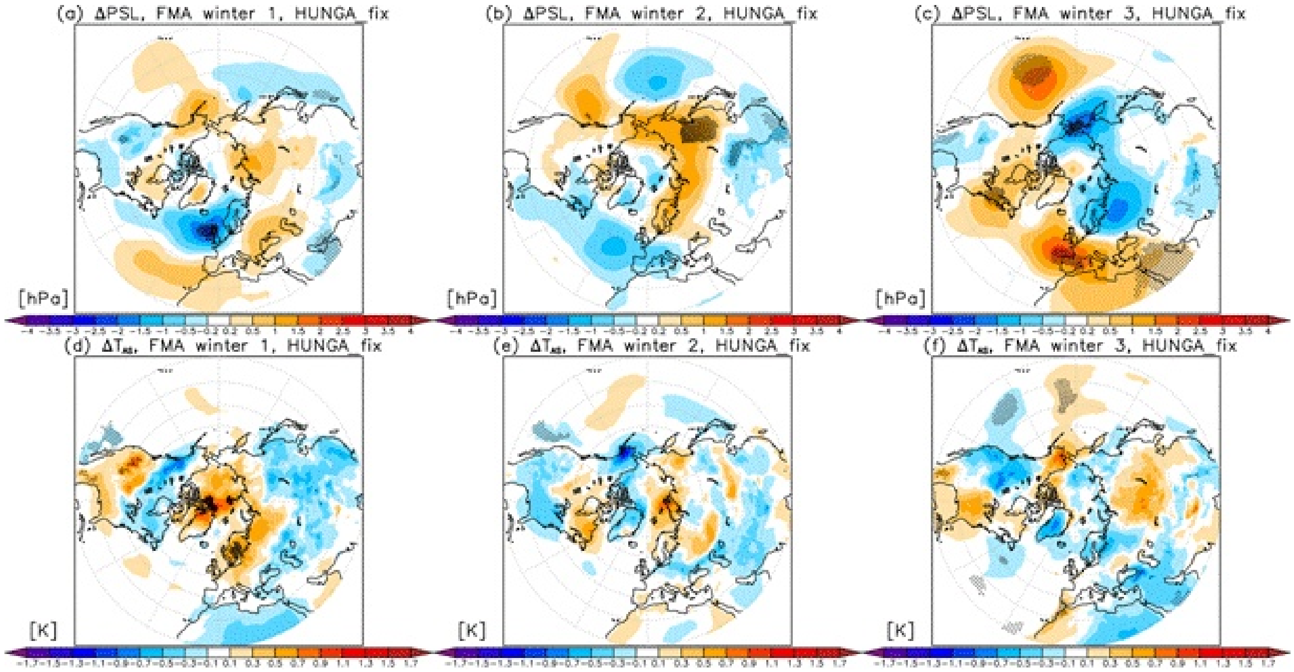

Figure S3.32: *As in Figure S3.31, but for years 5–10 in the atmosphere-only simulations.*

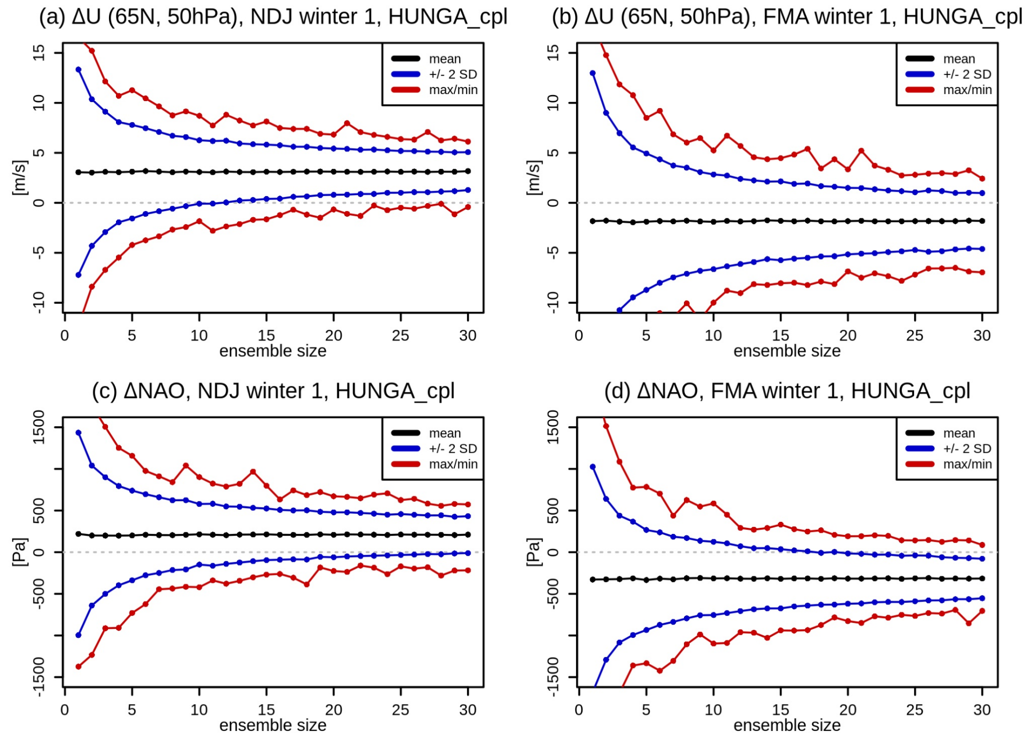

__Figure S3.33:__ Detectability of the early winter (a,c) and late winter (b,d) NH stratospheric vortex (a,b) and NAO (c,d) responses in the coupled ocean simulations during the first winter following the eruption (2022/2023). Black lines denote the mean response; blue and red lines indicate the ±2 standard deviation and maximum/minimum ranges, respectively, obtained by randomly subsampling the ensemble with replacement to generate 2000 artificial ensembles for each ensemble size.

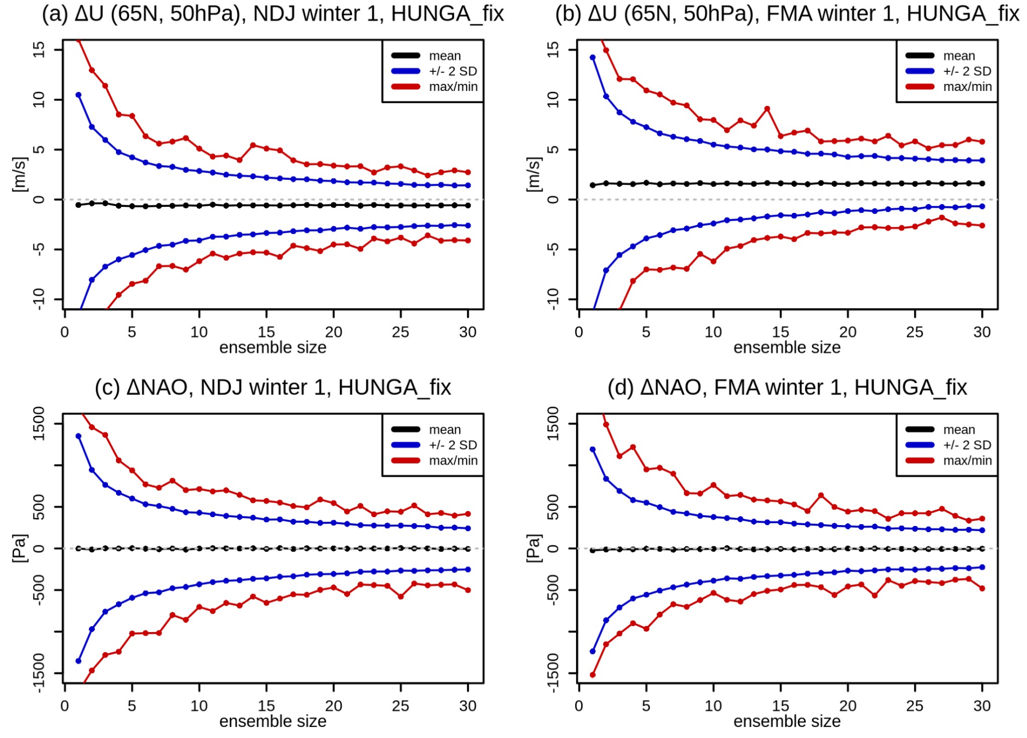

__Figure S3.34:__ As in Figure S3.33, but for the detectability of the changes in the atmosphere-only simulations.

S3.4.3 Seasonal changes in the SH polar vortex and impacts on the extratropical surface climate

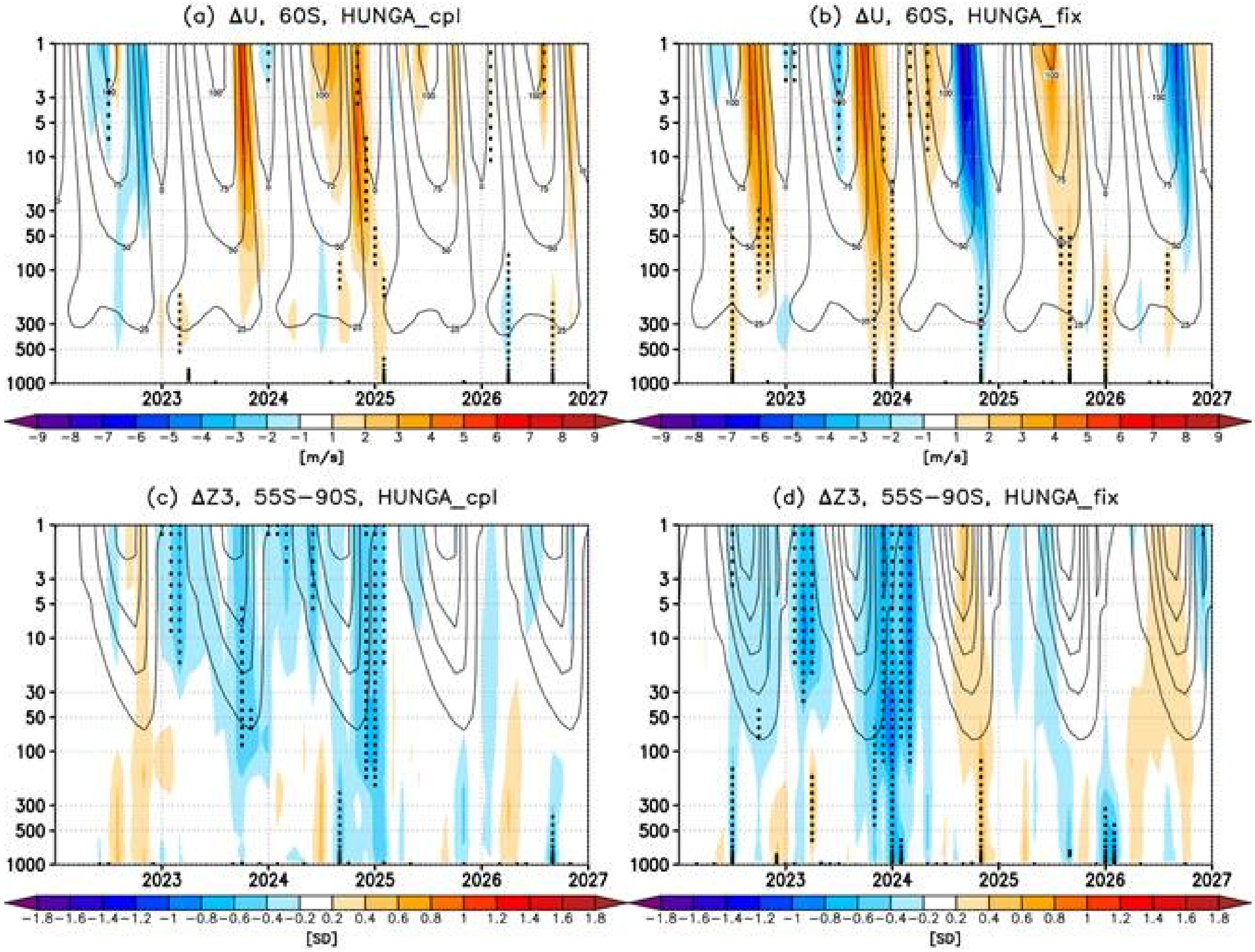

Figure S3.35: *Evolution of the Southern Hemisphere (SH) polar vortex. Shading: time series of changes in (a–b) zonal wind at 60°S (in* $\mathrm{m\,s^{-1}}$*) and (c–d) geopotential height (in standard deviations) averaged over the Antarctic polar cap (55°–90°S) between the forced simulation and the control. Left panels correspond to the coupled ocean simulations, right panels to the atmosphere-only simulations. Stippling denotes regions where the response is statistically significant (defined as in Figure S3.23).*

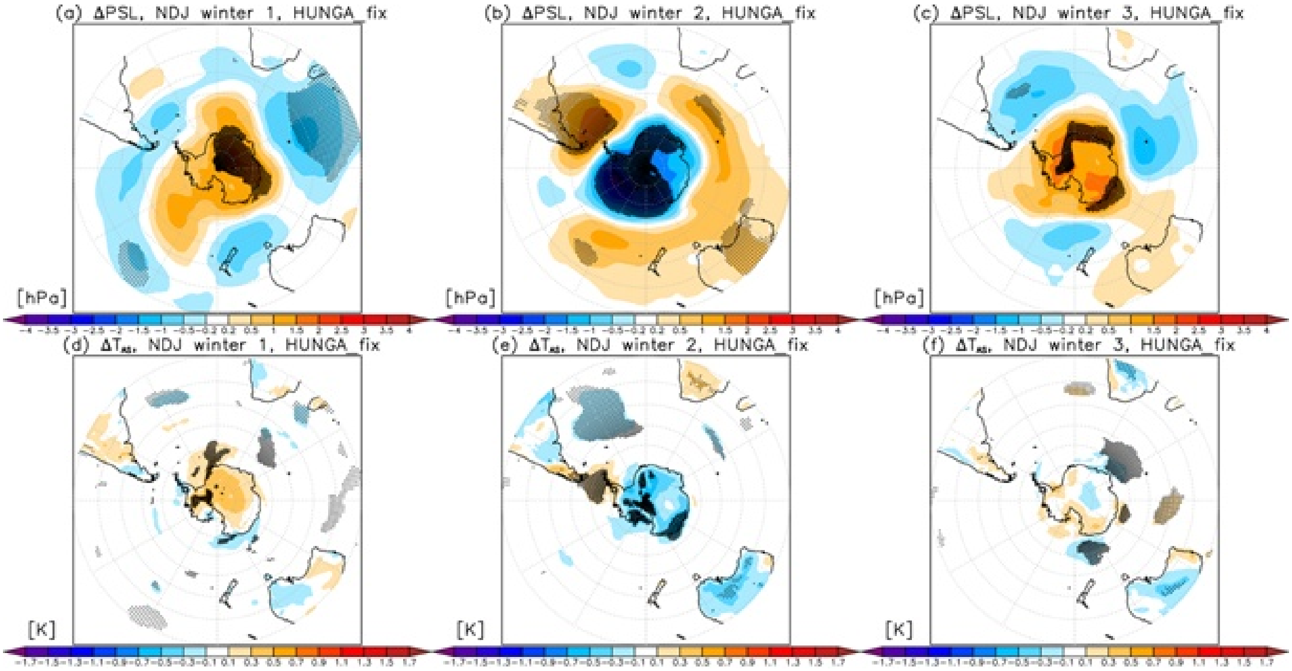

Figure S3.36: *Changes in late austral spring and early summer (November–December–January) (top) sea-level pressure and (bottom) near-surface air temperature between the forced simulation and the control in the atmosphere-only simulations for the first (2022/2023), second (2023/2024), and third (2024/2025) years following the eruption (columns). Stippling denotes statistical significance (defined as in Figure S3.23).*

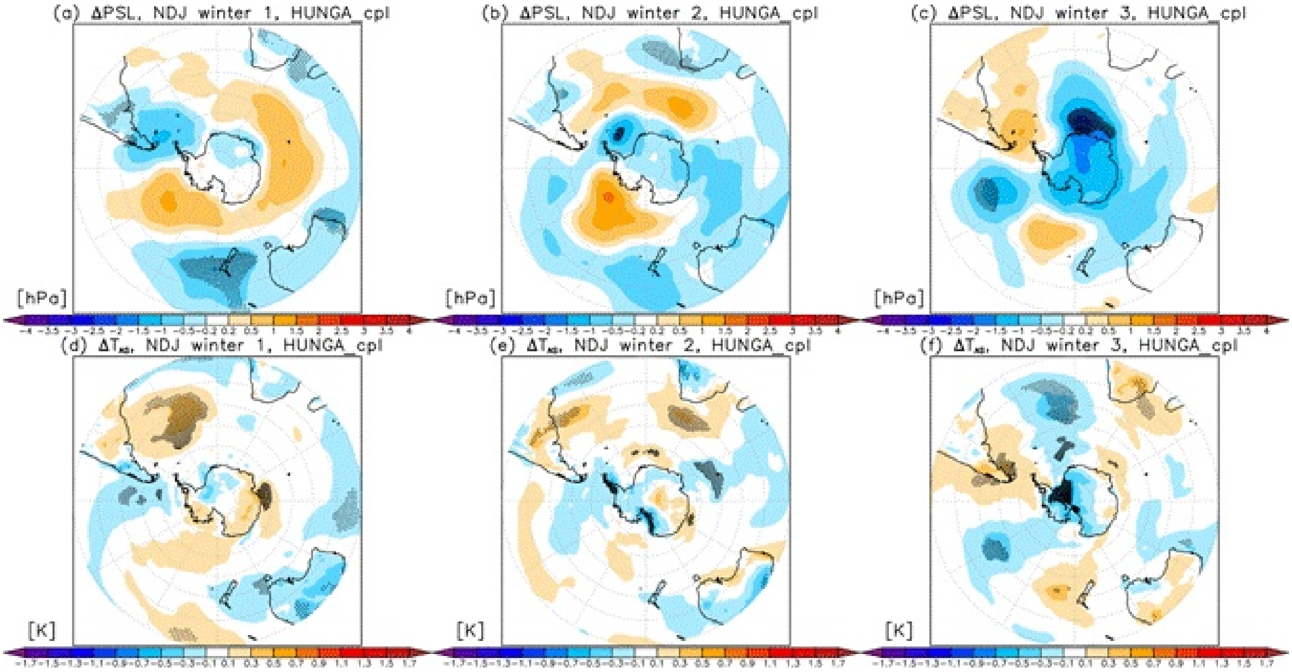

Figure S3.37: *As in Figure S3.36, but for the changes in the coupled ocean simulations.*

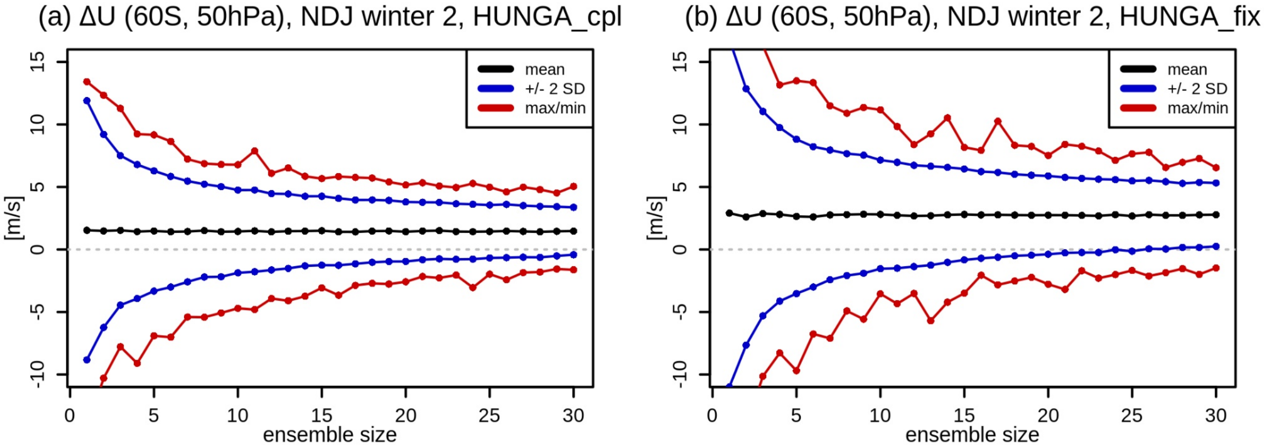

Figure S3.38: *Detectability of the changes in the 2023–2024 November–December–January SH lower stratospheric vortex in the coupled ocean (a) and atmosphere-only (b) simulations. Different lines correspond to those shown in Figure S3.33.*

S3.5 Upper stratosphere to thermosphere effects and H_2O transport in the deep Brewer–Dobson branch: modelling of long-term middle-atmospheric impacts

Authors Wandi Yu
Jia Yue
Yunqian Zhu
Xinyue Wang
Simone Tilmes
Jun Zhang
Zhihong Zhuo
Ewa M. Bednarz
Eric Fleming
David Plummer

This section analyses the upper-stratospheric to thermospheric responses to the Hunga eruption using multi-model ensemble simulations. The analysis focuses on changes in large-scale circulation, wave-driven transport, and water vapour propagation through the deep Brewer–Dobson branch, highlighting their long-term implications for the middle and upper atmosphere.

Simulations are based on 60-member WACCM6MAM Exp4 ensembles (30 with fixed SSTs/sea-ice and 30 with coupled ocean configurations) with combined H_2O and SO_2 injections, a 10-member CMAM ensemble (H_2O only), and a 20-member GSFC2D ensemble (H_2O and SO_2) conducted under fixed SSTs configuration.

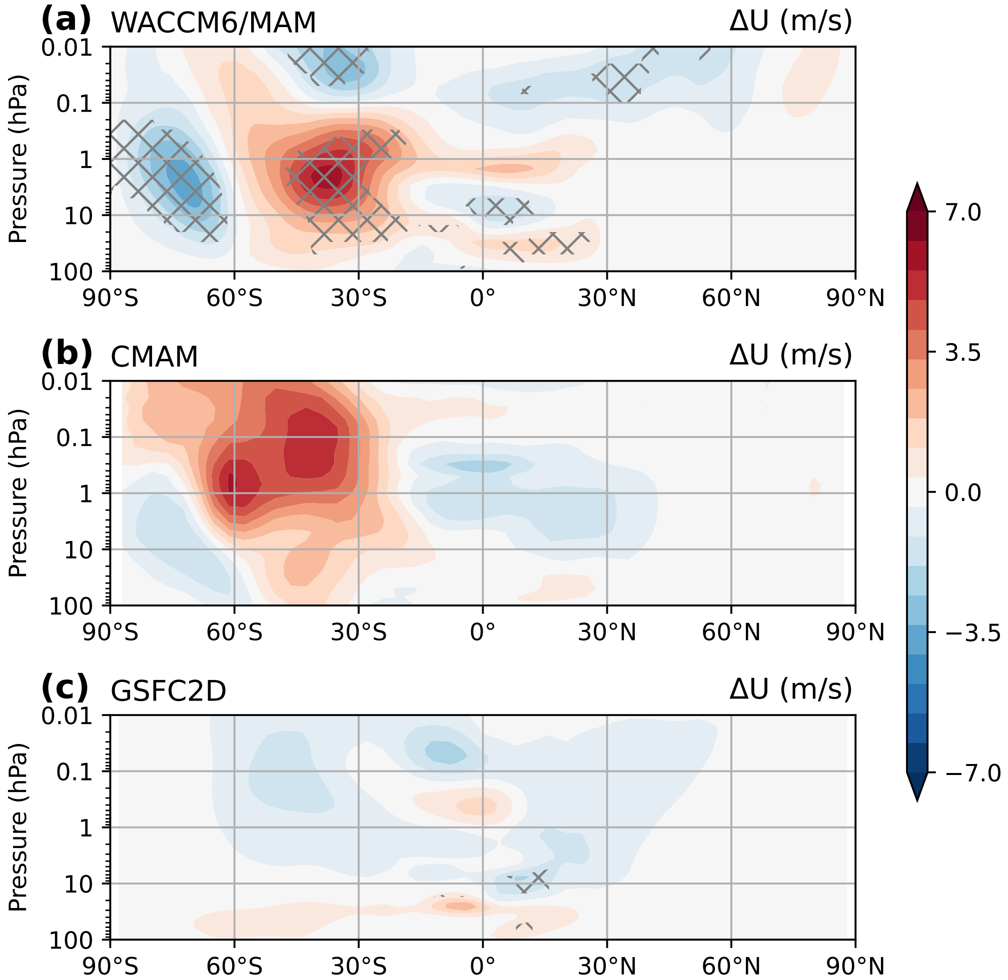

Figure S3.39: *Zonal mean zonal wind differences between the volcanic and control cases in July–August 2022, as simulated in (a) WACCM6MAM, (b) CMAM, and (c) GSFC2D. Areas with hatching indicate statistically significant differences.*

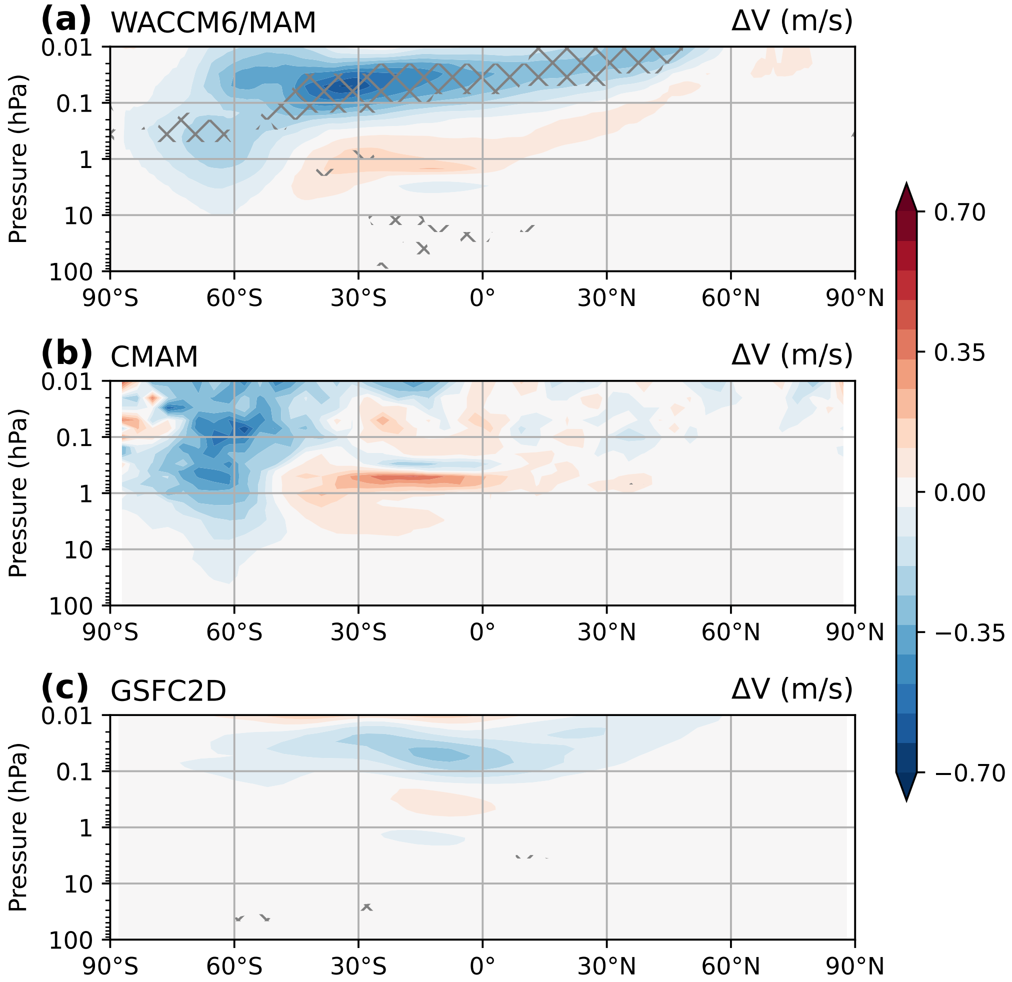

Figure S3.40: *Same as figure S3.39, but showing meridional wind differences between the volcanic and control simulations.*

S3.6 Simulated effects on total column ozone and halogen repartitioning in the Southern Hemisphere lower stratosphere

This section is based on: Bednarz et al. (2025a).

Bednarz, E. M., Aquila, V., Butler, A. H., Colarco, P., Fleming, E., Østerstrøm, F. F., Plummer, D., Quaglia, I., Randel, W., Santee, M. L., Sekiya, T., Tilmes, S., Wang, X., Watanabe, S., Yu, W., Zhang, J., Zhu, Y., and Zhuo, Z.: Multi-model assessment of impacts of the 2022 Hunga eruption on stratospheric ozone and its chemical and dynamical drivers, *EGUsphere [preprint]*, `https://doi.org/10.5194/egusphere-2025-4609`, 2025.

This section presents the modelled effects of the 2022 Hunga eruption on total column ozone and the partitioning of halogen species in the Southern Hemisphere (SH) lower stratosphere. The results are based on a coordinated multi-model analysis using GEOSCCM, MIROC-CHASER, and WACCM-MAM simulations, encompassing both free-running and specified-dynamics experiments. The experiments assess the combined and individual effects of sulfur dioxide (SO_2) and water vapour (H_2O) injections, as well as their direct chemical and radiative–dynamical impacts.

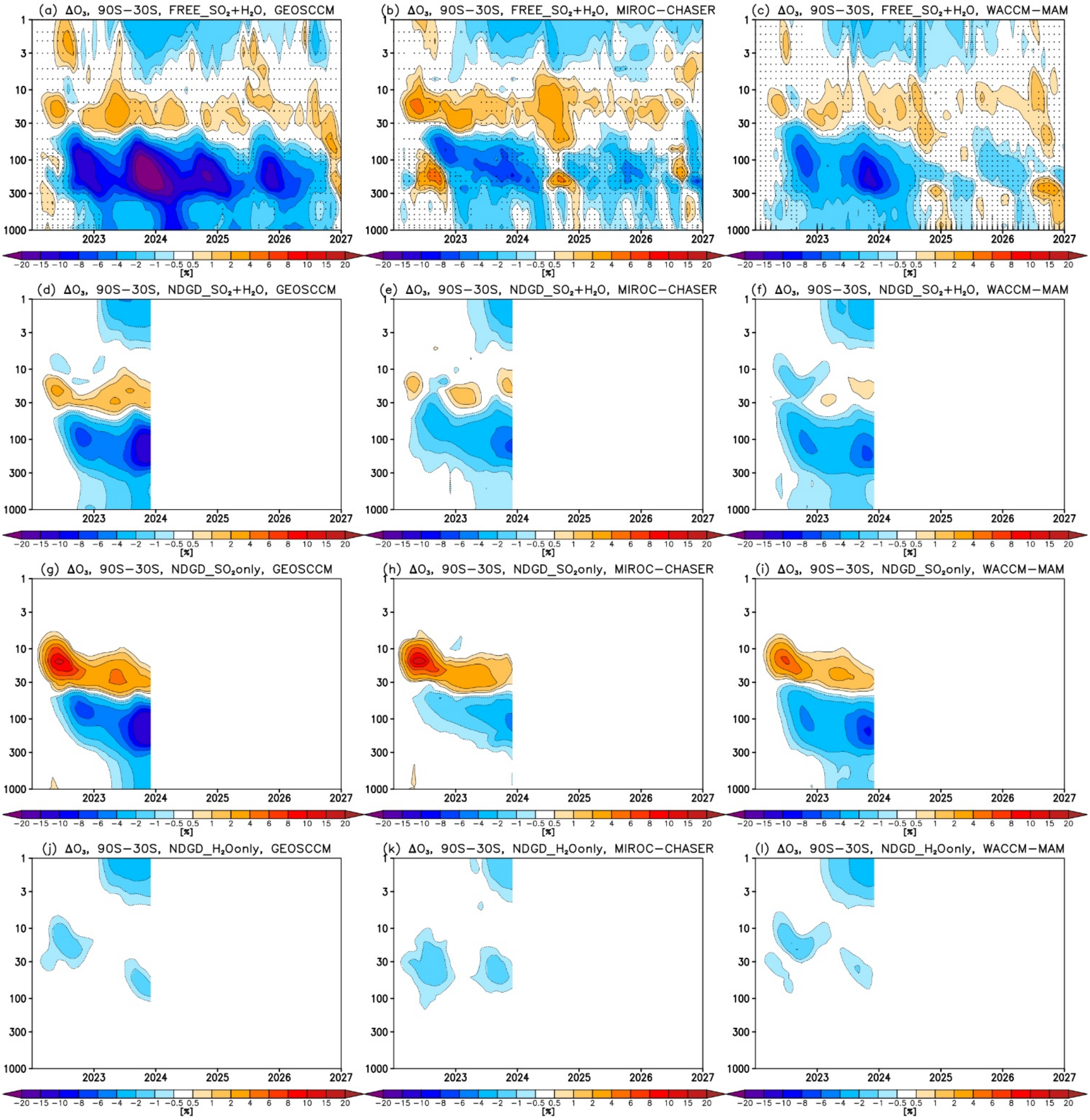

Figure S3.41: *Hunga-induced changes in SH extratropical (90°S–30°S) ozone mixing ratios, calculated as the differences (perturbed minus control) between simulations with and without Hunga forcing. Results are shown for GEOSCCM (a,d,g,j), MIROC-CHASER (b,e,h,k), and WACCM-MAM (c,f,i,l), with ensemble-mean responses displayed in all cases. (a–c) Free-running experiments including injection of both 0.5 Tg of SO_2 and ~150 Tg of H_2O (FREE_SO_2+H_2O). Stippling marks regions where the response in ozone is not statistically significant. (d–f) Specified-dynamics experiments with nudged meteorological fields (MERRA-2) including both SO_2 and H_2O injections (NDGD_SO_2+H_2O). Since the meteorology is identical for perturbed and control runs, these quantify direct chemical effects only. (g–i) Experiments with SO_2-only injections (NDGD_SO_2ONLY); (j–l) experiments with H_2O-only injections (NDGD_H_2OONLY). The bottom two rows isolate the effects of aerosol and water vapour perturbations from Hunga.*

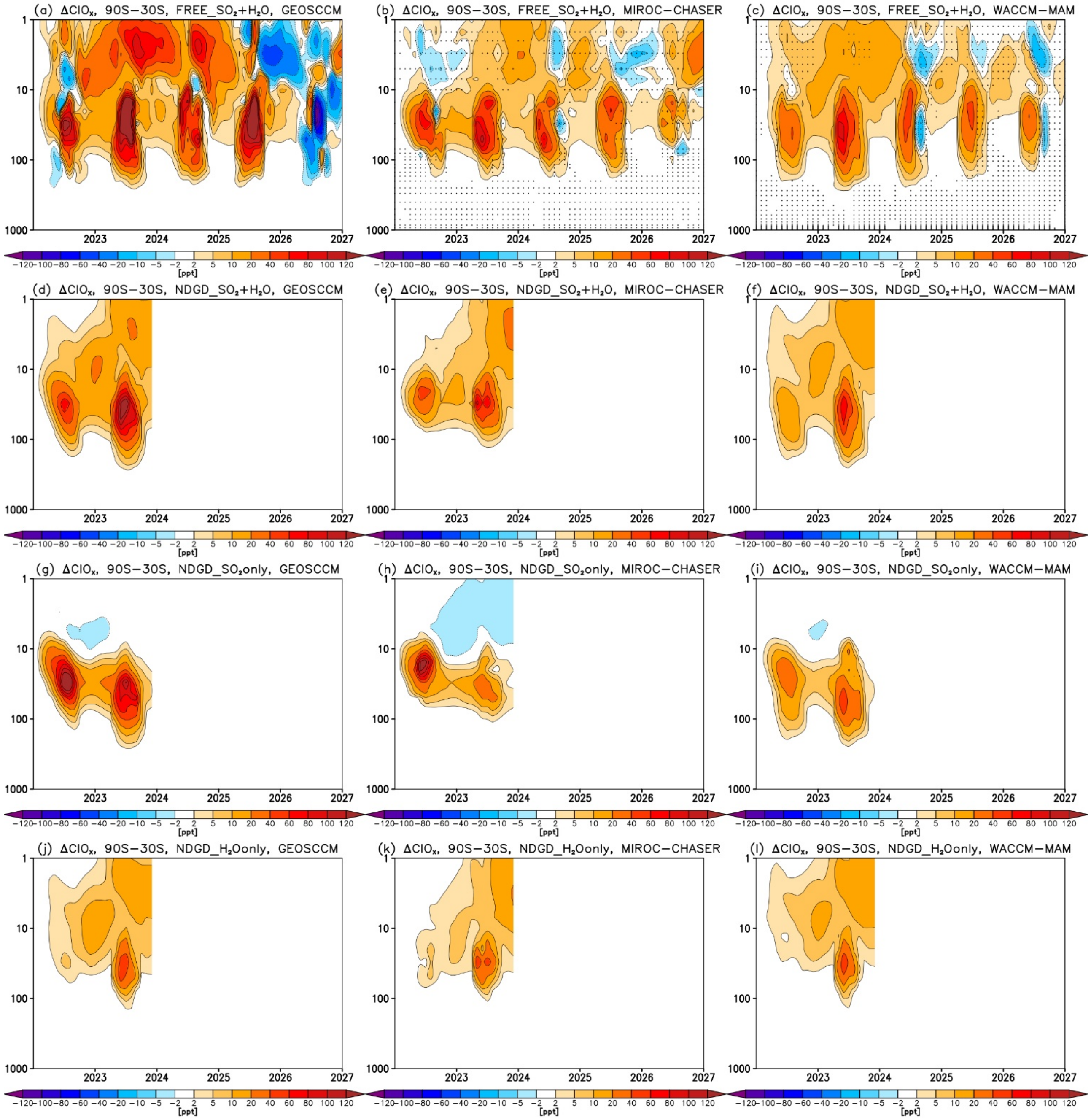

Figure S3.42: *As in Figure S3.41, but showing changes in ClO$_x$ (Cl + ClO + 2 × ClOOCl + HOCl + OClO + 2 × Cl$_2$) mixing ratios.*

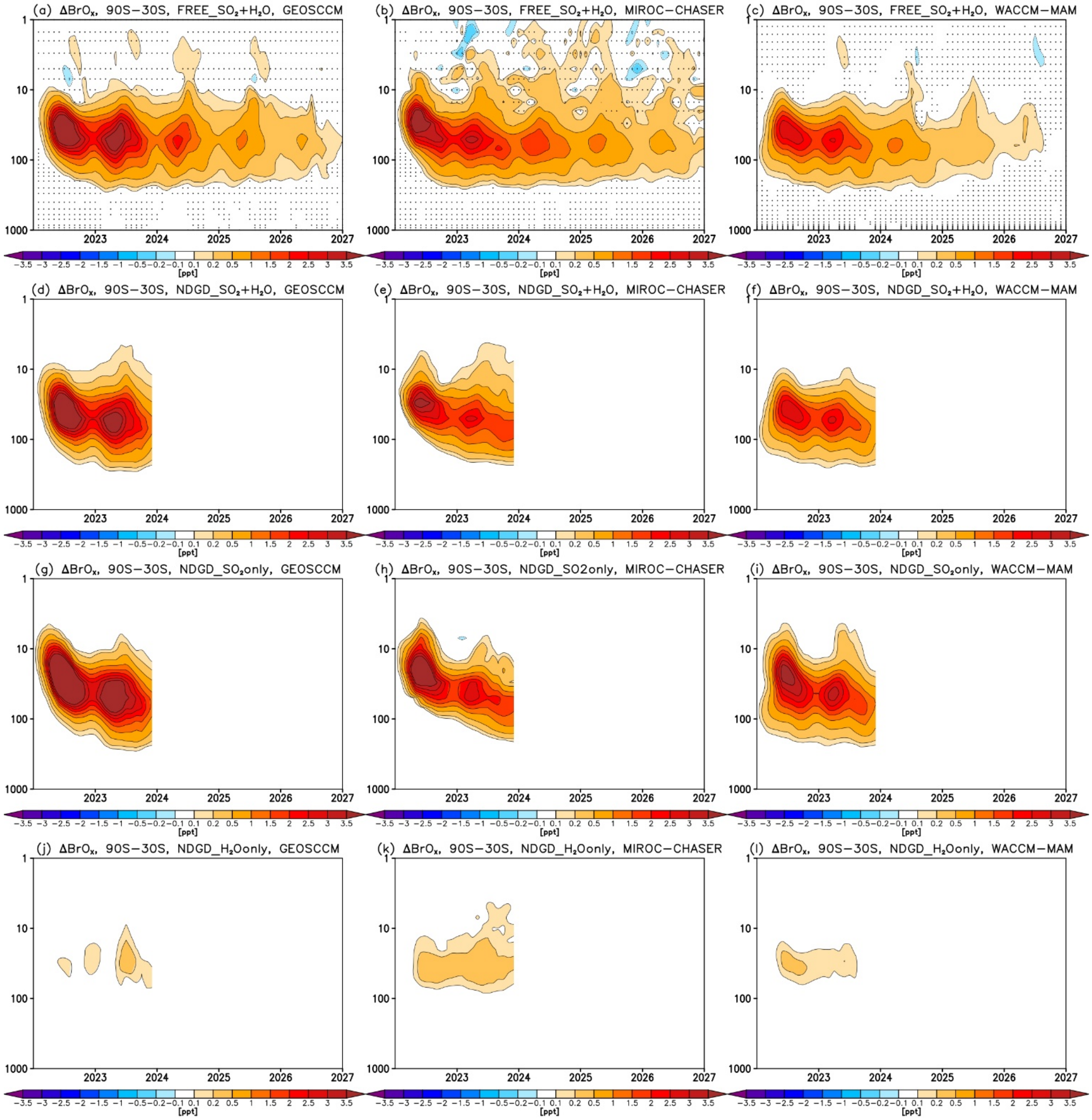

Figure S3.43: *As in Figure S3.41, but showing changes in* BrO_x *(Br + BrO + BrCl + HOBr) mixing ratios.*

References

Bednarz, E. M., V. Aquila, A. H. Butler, P. Colarco, E. Fleming, F. F. Østerstrøm, D. Plummer, I. Quaglia, W. Randel, M. L. Santee et al. (2025a). 'Multi-model assessment of impacts of the 2022 Hunga eruption on stratospheric ozone and its chemical and dynamical drivers'. *EGUsphere [preprint]*, 2025, pp. 1–24. DOI: `10.5194/egusphere-2025-4609`.

Bednarz, E. M., A. H. Butler, X. Wang, Z. Zhuo, W. Yu, G. Stenchikov, M. Toohey and Y. Zhu (2025b). 'Indirect climate impacts of the Hunga eruption'. *EGUsphere [preprint]*, DOI: `10.5194/egusphere-2025-1970`.

Butchart, N. (2014). 'The Brewer-Dobson circulation'. *Rev. Geophys.*, 52, pp. 157–184. DOI: `10.1002/2013rg000448`.

Carr, J. L., Á. Horváth, D. L. Wu and M. D. Friberg (2022). 'Stereo Plume Height and Motion Retrievals for the Record-Setting Hunga Tonga-Hunga Ha'apai Eruption of 15 January 2022'. *Geophys. Res. Lett.*, 49, e2022GL098131. DOI: `10.1029/2022gl098131`.

Clyne, M., O. B. Toon, T. Sukhodolov, G. W. Mann, S. Dhomse, S. Tilmes, Y. Zhu, P. R. Colarco, K. Tsigaridis, T. Nagashima et al. (2024). 'Tonga-MIP: The Hunga Tonga-Hunga Ha'apai Volcano Model Intercomparison Project'. In M. Clyne (Ed.), *Modeling the role of volcanoes in the climate system* (Publication No. 31487034), `https://www.proquest.com/dissertations-theses/modeling-role-volcanoes-climate-system/docview/3100397790/se-2`. PhD thesis. University of Colorado at Boulder.

Evan, S., J. Brioude, K. H. Rosenlof, R.-S. Gao, R. W. Portmann, Y. Zhu, R. Volkamer, C. F. Lee, J.-M. Metzger, K. Lamy et al. (2023). 'Rapid ozone depletion after humidification of the stratosphere by the Hunga Tonga eruption'. *Science*, 382, eadg2551. DOI: `10.1126/science.adg2551`.

Fleming, E. L., P. A. Newman, Q. Liang and L. D. Oman (2024). 'Stratospheric Temperature and Ozone Impacts of the Hunga Tonga-Hunga Ha'apai Water Vapor Injection'. *J. Geophys. Res.*, 129, e2023JD039298. DOI: `10.1029/2023jd039298`.

Manney, G. L., M. L. Santee, A. Lambert, L. F. Millán, K. Minschwaner, F. Werner, Z. D. Lawrence, W. G. Read, N. J. Livesey and T. Wang (2023). 'Siege in the Southern Stratosphere: Hunga Tonga-Hunga Ha'apai Water Vapor Excluded From the 2022 Antarctic Polar Vortex'. *Geophys. Res. Lett.*, 50. DOI: `10.1029/2023gl103855`.

Millán, L., W. G. Read, M. L. Santee, A. Lambert, G. L. Manney, J. L. Neu, M. C. Pitts, F. Werner, N. J. Livesey and M. J. Schwartz (2024). 'The Evolution of the Hunga Hydration in a Moistening Stratosphere'. *Geophys. Res. Lett.*, 51, e2024GL110841. DOI: `10.1029/2024gl110841`.

Millán, L., M. L. Santee, A. Lambert, N. J. Livesey, F. Werner, M. J. Schwartz, H. C. Pumphrey, G. L. Manney, Y. Wang, H. Su et al. (2022). 'The Hunga Tonga-Hunga Ha'apai Hydration of the Stratosphere'. *Geophys. Res. Lett.*, 49, e2022GL099381. DOI: `10.1029/2022gl099381`.

Niemeier, U., S. Wallis, C. Timmreck, T. van Pham and C. von Savigny (2023). 'How the Hunga Tonga—Hunga Ha'apai Water Vapor Cloud Impacts Its Transport Through the Stratosphere: Dynamical and Radiative Effects'. *Geophys. Res. Lett.*, 50, e2023GL106482. DOI: `10.1029/2023gl106482`.

Quaglia, I., D. Visioni, E. M. Bednarz, Y. Zhu, G. Stenchikov, V. Aquila, C.-C. Liu, G. W. Mann, Y. Peng, T. Sekiya et al. (2025). 'Multi-model analysis of the radiative impacts of the 2022 Hunga eruption indicates a significant cooling contribution from the volcanic plume'. *EGUsphere [preprint]*, 2025, pp. 1–35. DOI: `10.5194/egusphere-2025-3769`.

Randel, W. J., X. Wang, J. Starr, R. R. Garcia and D. Kinnison (2024). 'Long-Term Temperature Impacts of the Hunga Volcanic Eruption in the Stratosphere and Above'. *Geophys. Res. Lett.*, 51. DOI: `10.1029/2024gl111500`.

Santee, M. L., A. Lambert, L. Froidevaux, G. L. Manney, M. J. Schwartz, L. F. Millán, N. J. Livesey, W. G. Read, F. Werner and R. A. Fuller (2023). 'Strong Evidence of Heterogeneous Processing on Stratospheric Sulfate Aerosol in the Extrapolar Southern Hemisphere Following the 2022 Hunga Tonga-Hunga Ha'apai Eruption'. *J. Geophys. Res.*, 128, e2023JD039169. DOI: `10.1029/2023jd039169`.

Schoeberl, M. R., Y. Wang, G. Taha, D. J. Zawada, R. Ueyama and A. Dessler (2024). 'Evolution of the Climate Forcing During the Two Years After the Hunga Tonga-Hunga Ha'apai Eruption'. *J. Geophys. Res.*, 129, e2024JD041296. DOI: `10.1029/2024jd041296`.

Taha, G., R. Loughman, P. R. Colarco, T. Zhu, L. W. Thomason and G. Jaross (2022). 'Tracking the 2022 Hunga Tonga-Hunga Ha'apai Aerosol Cloud in the Upper and Middle Stratosphere Using Space-Based Observations'. *Geophys. Res. Lett.*, 49, e2022GL100091. DOI: `10.1029/2022gl100091`.

Wang, X., W. Randel, Y. Zhu, S. Tilmes, J. Starr, W. Yu, R. Garcia, O. B. Toon, M. Park, D. Kinnison et al. (2023). 'Stratospheric Climate Anomalies and Ozone Loss Caused by the Hunga Tonga-Hunga Ha'apai Volcanic Eruption'. *J. Geophys. Res.*, 128, e2023JD039480. DOI: `10.1029/2023jd039480`.

Wilmouth, D. M., F. F. Østerstrøm, J. B. Smith, J. G. Anderson and R. J. Salawitch (2023). 'Impact of the Hunga Tonga volcanic eruption on stratospheric composition'. *Proc. Natl. Acad. Sci.*, 120, e2301994120. DOI: `10.1073/pnas.2301994120`.

Zhang, J., D. Kinnison, Y. Zhu, X. Wang, S. Tilmes, K. Dube and W. Randel (2024). 'Chemistry Contribution to Stratospheric Ozone Depletion After the Unprecedented Water-Rich Hunga Tonga Eruption'. *Geophys. Res. Lett.*, 51, e2023GL105762. DOI: `10.1029/2023gl105762`.

Zhou, X., S. S. Dhomse, W. Feng, G. Mann, S. Heddell, H. Pumphrey, B. J. Kerridge, B. Latter, R. Siddans, L. Ventress et al. (2024). 'Antarctic Vortex Dehydration in 2023 as a Substantial Removal Pathway for Hunga Tonga-Hunga Ha'apai Water Vapor'. *Geophys. Res. Lett.*, 51, e2023GL107630. DOI: `10.1029/2023gl107630`.

Zhu, Y., H. Akiyoshi, V. Aquila, E. Asher, E. M. Bednarz, S. Bekki, C. Brühl, A. H. Butler, P. Case, S. Chabrillat et al. (2025). 'Hunga Tonga–Hunga Ha'apai Volcano Impact Model Observation Comparison (HTHH-MOC) project: experiment protocol and model descriptions'. *Geosci. Model Dev.*, 18, pp. 5487–5512. DOI: `10.5194/gmd-18-5487-2025`.

Zhu, Y., C. G. Bardeen, S. Tilmes, M. J. Mills, X. Wang, V. L. Harvey, G. Taha, D. Kinnison, R. W. Portmann, P. Yu et al. (2022). 'Perturbations in stratospheric aerosol evolution due to the water-rich plume of the 2022 Hunga-Tonga eruption'. *Commun. Earth Environ.*, 3, 248. DOI: `10.1038/s43247-022-00580-w`.

Zhu, Y., R. W. Portmann, D. Kinnison, O. B. Toon, L. Millán, J. Zhang, H. Vömel, S. Tilmes, C. G. Bardeen, X. Wang et al. (2023). 'Stratospheric ozone depletion inside the volcanic plume shortly after the 2022 Hunga Tonga eruption'. *Atmos. Chem. Phys.*, 23, pp. 13355–13367. DOI: `10.5194/acp-23-13355-2023`.